Forecasts for detecting the gravitational-wave memory effect with Advanced LIGO and Virgo

Boersma, O.M.; Nichols, D.A.; Schmidt, P.

DOI
10.1103/PhysRevD.101.083026

Publication date
2020

Document Version
Final published version

Published in
Physical Review D

Forecasts for detecting the gravitational-wave memory effect with Advanced LIGO and Virgo

Oliver M. Boersma,[1,2,*] David A. Nichols,[3,4,2,†] and Patricia Schmidt[5,2,‡]

[1]*Anton Pannekoek Institute for Astronomy, University of Amsterdam, Science Park 904, P.O. Box 94249, 1090 GE Amsterdam, The Netherlands*
[2]*Department of Astrophysics, Faculty of Science, Radboud University Nijmegen, P.O. Box 9010, 6500 GL Nijmegen, The Netherlands*
[3]*Department of Physics, University of Virginia, 382 McCormick Road, P.O. Box 400714, Charlottesville, Virginia 22904-4714, USA*
[4]*Gravitation Astroparticle Physics Amsterdam (GRAPPA), University of Amsterdam, Science Park 904, P.O. Box 94485, 1090 GL Amsterdam, The Netherlands*
[5]*School of Physics and Astronomy and Institute for Gravitational Wave Astronomy, University of Birmingham, Edgbaston B15 2TT, United Kingdom*

(Received 5 February 2020; accepted 4 March 2020; published 22 April 2020)

The detection of gravitational waves (GWs) from binary black holes (BBHs) has allowed the theory of general relativity to be tested in a previously unstudied regime: that of strong curvature and high GW luminosities. One distinctive and measurable effect associated with this aspect of the theory is the nonlinear GW memory effect. The GW memory effect is characterized by its effect on freely falling observers: the proper distance between their locations differs before and after a burst of GWs passes by their locations. Gravitational-wave interferometers, like the LIGO and Virgo detectors, can measure features of this effect from a single BBH merger, but previous work has shown that it will require an event that is significantly more massive and closer than any previously detected GW event. Finding evidence for the GW memory effect within the entire population of BBH mergers detected by LIGO and Virgo is more likely to occur sooner. A prior study has shown that the GW memory effect could be detected in a population of BBHs consisting of binaries like the first GW150914 event after roughly one-hundred events. In this paper, we compute forecasts of the time it will take the Advanced LIGO and Virgo detectors (when the detectors are operating at their design sensitivities) to find evidence for the GW memory effect in a population of BBHs that is consistent with the measured population of events in the first two observing runs of the LIGO detectors. We find that after five years of data collected by the Advanced LIGO and Virgo detectors the signal-to-noise ratio for the nonlinear GW memory effect in the population will be about three (near a previously used threshold for detection). We point out that the different approximation methods used to compute the GW memory effect can lead to notably different signal-to-noise ratios.

DOI: 10.1103/PhysRevD.101.083026

I. INTRODUCTION

The first detection of a gravitational waves (GWs) from a pair of merging black holes (GW150914) by the LIGO detectors [1] opened a new avenue for testing the predictions of general relativity for strongly gravitating and rapidly evolving spacetimes. The observed GWs were consistent with the predictions of general relativity (GR) to within the statistical uncertainties of the measurement [2]. The LIGO, and subsequently Virgo, detectors have continued to discover new GW events: after the first two observing runs of the two LIGO detectors now ten GWs from binary-black-hole (BBH) mergers and one from a binary-neutron-star merger have been discovered [3]. (The GWs from these ten additional events are also consistent with the predictions of GR [4].) Already in the third observing run of LIGO, over 20 BBH candidate events have been announced [5] and this number will rapidly increase once the detectors reach their design sensitivities in a few years [6]. The improved sensitivity of the detectors and the large number of events will allow GR to be tested more precisely for a range of binaries with different masses and spins.

Before the LIGO and Virgo discoveries, the predictions of GR were consistent with a range of experiments and measurements in the Solar System and through observations of pulsars in the Milky Way (see, e.g., [7] for a review). Solar System, pulsar, and BBH observations probe

*o.m.boersma@uva.nl
†david.nichols@virginia.edu
‡pschmidt@star.sr.bham.ac.uk

different aspects of Einstein's theory: most importantly, BBHs allow GR to be studied in a more nonlinear and highly radiating regime of the theory than either Solar System experiments or pulsar observations. Thus, BBHs will allow the study of gravitational phenomena that require nonlinearities and high GW luminosities. One such effect, called the nonlinear GW memory effect [8,9], is the focus of this paper.

The GW memory effect is characterized by a lasting change in the GW strain that occurs for many types of transient GW sources. Zel'dovich and Polnarev [10] first computed the GW memory effect in linearized gravity when they computed the GWs emitted by the gravitational scattering of compact objects.[1] The high luminosities of neutrinos from supernovae also can produce the GW memory effect, as was shown by Epstein [12] and Turner [13]. Christodoulou [8] showed that there is also a nonlinear contribution to the effect in the full theory of GR (without the linear approximation), which arises from the energy flux (luminosity per solid angle) from the GWs. Blanchet and Damour [9] independently computed the effect within the context of the multipolar-expanded post-Minkowskian approximation. Binary black holes, with their high GW luminosities, are expected to have a non-negligible GW memory effect (see, e.g., [14,15] for calculations in post-Newtonian theory and [16] for computations of the GW memory in numerical-relativity simulations).

The GW memory effect can be measured, because when a GW with memory passes by freely falling observers, the proper displacement between the observers differs before and after the burst of GWs pass by their locations. The GW memory effect also has close connections to the symmetry group of asymptotically flat spacetimes, the Bondi-Metzner-Sachs group [17–19], and its corresponding conserved quantities (see, e.g., [20] for more details). Thus, because of its distinctive observational signature and its close connection to fundamental aspects of asymptotically flat spacetimes, the GW memory effect would be of great interest to detect.

The GW memory effect is formally the constant difference in the GW strain before and after a burst of GWs passes by a GW detector. Interferometric GW detectors like LIGO and Virgo, however, are sensitive to GWs over a finite frequency range; thus, they do not always have the necessary sensitivity at low frequencies to measure the lasting change in the GW strain associated with the memory. Nevertheless, the simulations in [16] confirmed the analytical approximation used in [21], which showed that the memory effect rapidly settles to a nonzero constant value over a timescale (and hence frequency range) that LIGO and Virgo can measure, for stellar-mass BBHs. The prospects for measuring the GW memory effect from the full inspiral-merger-ringdown waveform of a BBH showed more promise for detecting the effect than earlier studies using just the post-Newtonian approximation to the waveform during the inspiral [22,23]. However, Favata [21] and more recently Johnson *et al.* [24] showed that for LIGO and Virgo to detect the GW memory from a single BBH merger would require a much closer or more massive BBH event than had previously been observed. Next-generation ground-based detectors such as the Einstein Telescope [25] and Cosmic Explorer [26] were shown in [24] to be much more likely to detect the GW memory effect. The planned space-based GW detector, LISA [27], could detect the GW memory from supermassive BBH mergers (see, e.g., [21]). Pulsar timing arrays (see, e.g., [28]) have also put constraints on GWs with memory (see [29] and references therein), though there are forecasts that suggest pulsar timing arrays are less likely than LISA is to detect the GW memory effect [30].

Instead of searching for the GW memory effect associated with a single BBH merger, Lasky *et al.* [31] proposed to search for evidence for the GW memory effect in a population of BBH mergers, for which each individual event is below the threshold for detection. Lasky *et al.* showed that for a population of GW150914-like events, around 100 BBH mergers are needed to find evidence for the GW memory effect in the population. An important insight in [31] was that only a subset of mergers in the population can be used to build evidence for the GW memory effect, because of degeneracies of certain "extrinsic" parameters (parameters that are *not* the masses or spins of the black holes) in the detectors' responses to the GWs. Moreover, a criteria (which can be computed from the GWs) was found in [31] to determine whether a given detection would be likely to contribute evidence for the GW memory in the population or not.

In this paper, we revisit the forecasts in [31] in light of the nine additional BBH detections after the GW150914 event. The first ten detections have now allowed models of the distribution of BBH masses to be constrained by observational data [32]. We use populations of BBHs consistent with these models to estimate the amount of time the Advanced LIGO and Virgo detectors will need to detect the GW memory effect in these populations.[2] We find that, on average, after a five-year observation period, the signal-to-noise ratio for the GW memory effect in the population of BBHs will be about three (near the threshold to be observed). There have been a number of different approximations used to compute the GW memory effect

[1]Note that the possibility of the GW memory effect was considered by Newman and Penrose in [11], although they did not explicitly calculate the effect from any source.

[2]As this work was coming to completion, related forecasts for the number of events needed to detect the GW memory effect were made in [33]. We discuss the relationship between [33] and this paper in greater detail in the note added after the acknowledgments.

from BBH mergers (see, e.g., [21,24,34,35]). We caution that these models can differ in their predictions for the amplitude of the memory effect, and this does have an impact on the signal-to-noise for the memory effect in our populations.

The remainder of this article is structured as follows: In Sec. II, we describe how we calculate the relevant gravitational waveforms used throughout this paper. Section III describes our data-analysis procedures. Section IV contains the main results of our study: the criteria to determine when a BBH merger will contribute to building evidence for the memory in the population, and the forecasts for the time to detection for the GW memory effect in our simulated populations of BBHs. We conclude in Sec. V. A few additional results are given in Appendices A–C. In the remainder of this article geometric units $G = c = 1$ are used. We use the Planck 2015 [36] cosmology to associate a luminosity distance of a BBH to its redshift.

II. GRAVITATIONAL WAVEFORM MODELS

In this section, we discuss several different aspects of the gravitational waveform models we use throughout this paper: (i) the conventions for the multipolar expansion of the GW polarizations, (ii) the specific waveform approximants we use in this paper, (iii) the procedure used to calculate the waveform associated with the nonlinear GW memory effect, (iv) the effect of using different waveform approximants in the procedure of (iii), and (v) a degeneracy among certain extrinsic parameters in the waveform.

A. Gravitational waveforms and their spin-weighted spherical-harmonic expansion

Gravitational-wave detectors, such as LIGO and Virgo, are not equally sensitive to the two polarizations of the GWs, which come from different locations on the sky. The sensitivity of the detector to the plus and cross polarizations of the gravitational waveform (denoted by h_+ and $h_\times$, respectively) is given by two antenna response functions, $F_+(\alpha, \delta, \psi)$ and $F_\times(\alpha, \delta, \psi)$, which we parametrize by the right ascension α, the declination δ, and the polarization angle ψ. [We use the conventions that $\alpha \in (0, 2\pi)$, $\delta \in (-\pi/2, \pi/2)$, and $\psi \in (0, \pi)$.] The time-dependent strain measured by the detector is expressed as the combination of the two polarizations:

$$h(t) = F_+(\alpha, \delta, \psi) h_+(t) + F_\times(\alpha, \delta, \psi) h_\times(t) \tag{2.1}$$

(see, e.g., Appendix B of [37]). The expressions for F_+ and $F_\times$ are taken from the LIGO Algorithm Library (LAL) [38].

For nonprecessing BBH systems, it is convenient to decompose the complex strain, $h_+ - i h_\times$, using a basis of spin-weighted spherical harmonics (with spin weight $s = -2$) that is adapted to the binary. We assume the binary is in the x-y plane, so that the orbital (and total) angular momentum points along the z axis. We denote the spin-weighted spherical harmonics by ${}^{(-2)}Y_{\ell m}(\iota, \phi_c)$. We choose our coordinates such that ι represents the angle between angular momentum and the line of sight to the detector, and ϕ_c is the angle between the x axis and the line of site to the detector projected into the plane of the binary. The conventions for the harmonics we use are those implemented in the GWSURROGATE package [39] (which are computed from recurrence relations given in Appendix B of [40]). The expansion is then given by

$$h_+ - i h_\times = \sum_{l=2}^{\infty} \sum_{m=-\ell}^{\ell} h_{lm}(t; \vec{\sigma}) {}^{(-2)}Y_{\ell m}(\iota, \phi_c), \tag{2.2}$$

where we have written the spherical-harmonic modes $h_{\ell m}$ of the gravitational waveform as a function of time t and a set of parameters $\vec{\sigma}$. For nonprecessing binaries, the parameters included in $\vec{\sigma}$ are the heavier BH mass m_1, the lighter BH mass m_2, the dimensionless BH spins χ_{1z} and χ_{2z} (which are assumed to be aligned or antialigned with the orbital angular momentum), and luminosity distance d_L.

This spherical-harmonic decomposition is useful, because for nonprecessing BBHs, the amplitudes of the different (ℓ, m) modes fall off rapidly with ℓ and the corresponding frequency of the mode is proportional to m (see, e.g., [41]). Modes with $m \neq 0$ are referred to as "oscillatory" modes. The dominant oscillatory mode is the quadrupole mode h_{22}, whereas the modes with $(\ell, |m|) \neq (2, 2)$ are notably smaller in their amplitudes, and are sometimes referred to as "subdominant" or "higher-order" modes. As we discuss in more detail later in this section, for the quasicircular, aligned-spin binaries considered in this paper, the GW memory effect that is computed using h_{22} can be expanded in just the two modes h_{20} and h_{40} (and the GW polarization associated with these modes is just the plus polarization) [34]. Thus, modes with $m = 0$ are sometimes called "memory" modes.[3] By parity, it can be shown that for the aligned-spin binaries considered in this paper the modes with $m < 0$ are related to the modes with $m > 0$ by the relation $h^*_{\ell,m} = (-1)^m h_{\ell,-m}$; thus, we will subsequently only refer to the modes with $m > 0$ and not their counterparts with $m < 0$ when discussing which modes we use.

Finally, we conclude this section with a few additional definitions that are less standard, but which will be useful later in this paper. Let us denote the plus and cross polarizations associated with a given mode h_{lm} as

$$h_+^{\ell m} := \mathrm{Re}\{h_{\ell m} {}^{(-2)}Y_{\ell m}\}, \tag{2.3a}$$

[3]Note, however, that this classification is based on the behavior of the waveform modes during the inspiral; during the merger and ringdown the $m = 0$ modes can have an oscillatory part, and the memory can appear in modes with $m \neq 0$.

$$h_{\times}^{\ell m} := -\mathrm{Im}\{h_{\ell m}{}^{(-2)}Y_{\ell m}\}. \tag{2.3b}$$

Similarly, let us define the strain measured by the detector for a particular mode h_{lm} as

$$h_{(lm)}(t) := F_{+}(\alpha,\delta,\psi)h_{+}^{lm}(t) + F_{\times}(\alpha,\delta,\psi)h_{\times}^{lm}(t). \tag{2.4}$$

Thus the full GW strain measured by the detector can be written as

$$h(t) = \sum_{\ell,m} h_{(lm)}(t). \tag{2.5}$$

While the quantities $h_{(lm)}(t)$ are not something that would be easily measurable by GW detectors like LIGO and Virgo for a single (ℓ, m) mode, they will be useful for explaining certain degeneracies that occur when the GWs measured by a GW detector are influenced predominantly by a few individual $h_{(lm)}(t)$ in the total strain $h(t)$.

B. Computing the oscillatory waveform modes

To compute the dominant and higher-order oscillatory waveform modes, we use the NRHybSur3dq8 surrogate model [42]. This model can be used to generate waveforms from BBHs with mass ratios q in the range $q = m_1/m_2 \leq 8$ and with aligned spins with magnitudes $|\chi_{1z}|, |\chi_{2z}| \leq 0.8$. The model was built from a catalog of spinning, nonprecessing numerical relativity (NR) simulations [43] that were "hybridized" [44] with post-Newtonian (PN) (see e.g., the review article [45] and references therein) and effective-one-body (EOB) waveforms [46,47]. The surrogate model is a type of interpolant (based on reduced-order modeling techniques [48–52]) that allows the waveform model to be rapidly evaluated with high accuracy in its range of validity.

We use the Python package GWSURROGATE [39] to evaluate the NRHybSur3dq8 surrogate model. This model includes (ℓ, m) modes with $2 \leq \ell \leq 4$ [though not the (4,0) or (4,1) modes] and the (5,5) mode. We restrict to generating the dominant mode h_{22} and the five higher-order modes h_{21}, h_{32}, h_{33}, h_{44} and h_{55}. We neglect the other modes, as they are either small or not well resolved in the NR simulations. We choose the duration of the waveform to be such that the h_{55} mode starts at a frequency of $f_0 = 10$ Hz, for all the binaries (of different masses) that we consider.

C. Computing the nonlinear GW memory

The GW memory effect can be computed from NR simulations using the technique of Cauchy-characteristic extraction (see, e.g., [53]) as was done in [16] for a few nonprecessing, equal-mass BBHs. The more commonly used methods of waveform extraction (and extrapolation), however, fail to resolve the effect (see, e.g., [43]). The memory effect is required by the conservation of supermomentum (the conserved quantity associated with the supertranslation symmetries of the Bondi-Metzner-Sachs group); thus, the memory can be computed approximately from the gravitational waveform model without the GW memory effect by determining the waveform required to maintain supermomentum conservation (see, e.g., [54–56]).

While supermomentum conservation provides the theoretical underpinning for the approximate method for computing the GW memory effect from waveforms without GW memory, the resulting prescription can be described in simpler terms: One can compute the nonlinear GW memory following the same procedure used to calculate linear memory from massless fields after replacing the material stress-energy tensor with the effective stress-energy tensor of gravitational waves [22]. The derivation of the result relies on solving the relaxed Einstein equations (in harmonic gauge), and has been given in several places (e.g., [14,15]); as a result, we do not rederive the result, but quote the final result instead.

The strain associated with the memory effect can be computed from the expression

$$h_{jk}^{\mathrm{TT,mem}} = \frac{4}{r}\int_{-\infty}^{u} du' \left[\int \frac{dE}{d\Omega' du'}\frac{n_j' n_k'}{1-\mathbf{n}'\cdot\mathbf{n}}\, d\Omega'\right]^{TT}. \tag{2.6}$$

In this expression, we have defined the retarded time u, the distance to the source r, the unit vector pointing from the source $\mathbf{n} = \mathbf{x}/r$, the solid-angle element $d\Omega$, and the GW luminosity per solid angle $dE/(dud\Omega)$. To relate the expression in Eq. (2.6) to the two polarizations of the GWs, it is necessary to contract Eq. (2.6) with the complex polarization tensor as follows:

$$h_{+}^{\mathrm{mem}} - ih_{\times}^{\mathrm{mem}} = h_{jk}^{\mathrm{TT,mem}}(e_{+}^{jk} - ie_{\times}^{jk}). \tag{2.7}$$

It is convenient to define the polarization tensors using a complex vector m_j^* (where $*$ denotes complex conjugation). In spherical coordinates, (ι, ϕ_c), the vector m_j^* is given by $m^{*j} = [(\partial_\iota)^j - i\sin\iota(\partial_{\phi_c})^j]/\sqrt{2}$, and the polarization tensor is then

$$e_{+}^{jk} - ie_{\times}^{jk} = m^{*j}m^{*k}. \tag{2.8}$$

For practical computations of the nonlinear memory effect, it is common to expand the energy flux in terms of the time derivatives of the GW strain expanded in spin-weighted spherical harmonics:

$$\frac{dE}{dud\Omega} = \frac{r^2}{16\pi}\sum_{\ell',\ell'',m',m''} \langle \dot{h}_{\ell' m'}\dot{h}^{*}_{\ell'' m''}\rangle {}^{(-2)}Y_{\ell' m'}{}^{(-2)}Y^{*}_{\ell'' m''}. \tag{2.9}$$

The angle brackets around the term $\dot{h}_{\ell' m'}\dot{h}^{*}_{\ell'' m''}$ mean to average over a few wavelengths of the radiation.

By substituting Eq. (2.9) into Eq. (2.6), the memory waveform becomes a sum over products of two spin-weighted spherical harmonics. However, it is then useful to expand $h_+^{\rm mem} - ih_\times^{\rm mem}$ in spin-weighted spherical harmonics as

$$h_+^{\rm mem} - ih_\times^{\rm mem} = \sum_{\ell,m} h_{\ell m}^{\rm mem\,(-2)} Y_{\ell' m'}, \tag{2.10}$$

so that the multipole moments $h_{\ell m}^{\rm mem}$ are functions of time that are determined by a double angular integral of products of three spin-weighted spherical harmonics. These integrals, although somewhat complicated, can be evaluated numerically (as was done in [35]). Alternately, the integral can be recast in terms of symmetric-trace-free tensors or scalar spherical harmonics and evaluated analytically (in terms of Clebsch-Gordon coefficients or Wigner 3-j symbols) [15,54,57].

We compute several approximate expressions for the polarizations in Eq. (2.10) in the next part of this section.

D. Memory waveform models

We describe in this part three different approximate methods that have been used to compute the GW memory effect from BBHs. Two of the models differ only in the number of spherical-harmonic modes included in the expansion of the GW luminosity in Eq. (2.9). The other model uses additional approximations that we will discuss in greater detail herein. We discuss one additional waveform model in Appendix A that is used to compute the GW memory effect in [24]. This model makes several additional approximations, which have the effects of decreasing the amplitude of the GW memory effect by a factor of roughly 2, and introducing a small oscillatory part that would not be expected in these particular spherical-harmonic modes of the memory effect. For these reasons, we do not include this model in the calculations in this part. In Fig. 1, we provide an example that shows that the three different approximations can lead to results that differ by several tens of a percent.

1. Descriptions of waveform models

a. Quadrupole approximation.—In [21], Favata considered the memory generated by the luminosity just from the spherical-harmonic mode h_{22} in the luminosity in Eq. (2.9). However, unlike previous work in the PN approximation (e.g., [14,23]), Ref. [21] used the full inspiral-merger-ringdown waveform for h_{22}, which was fit to results from a NR simulation. The angular integral in Eq. (2.6) can be performed straightforwardly in this approximation, and the GW memory is predominantly in the spherical-harmonic modes $h_{20}^{\rm mem}$ and $h_{40}^{\rm mem}$ (and is thus plus polarized).[4]

[4]Note that there can also be small contributions to the mode h_{44}, though this will be ignored in this approximation.

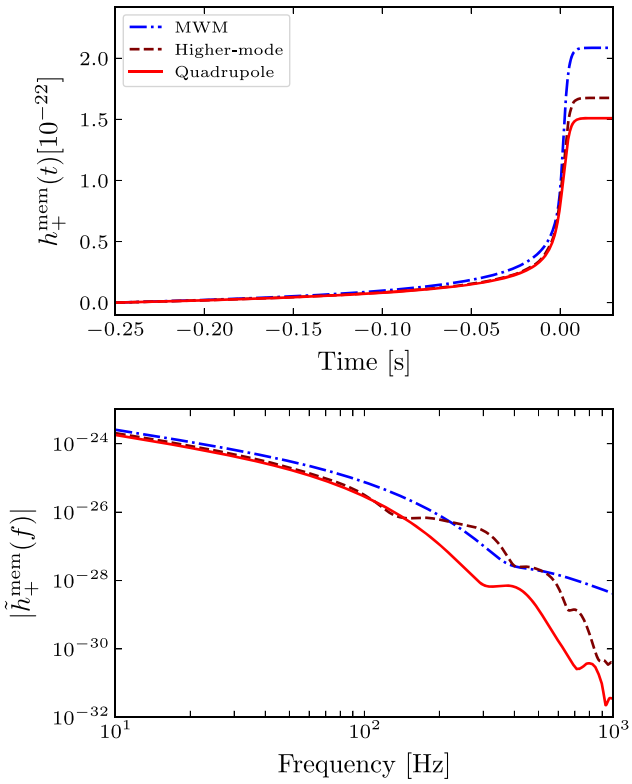

FIG. 1. Gravitational waveforms associated with the nonlinear GW memory effect for a BBH with masses $m_1 = 30M_\odot$ and $m_2 = 30M_\odot$, at a luminosity distance $d_L = 500$ Mpc and at an inclination $\iota = \pi/2$. The three curves are three different approximations for computing the GW memory waveform: the blue dot-dashed line is the MWM of [21], the red solid line is the quadrupole approximation also in [34], and the dashed brown line is the higher-mode model of [35] (see the text for more detailed descriptions of the models). Top: The time-domain waveform $h_+^{\rm mem}(t)$ for the nonlinear GW memory for the three models. Bottom: The nonlinear GW memory waveform in the frequency domain for the three models.

The resulting waveform for the plus polarization of the GW memory effect can be written as

$$h_+^{\rm mem}(u) = \frac{r}{192\pi}\sin^2\iota(17+\cos^2\iota)\int_{-\infty}^{u}|\dot{h}_{22}|^2 du'. \tag{2.11}$$

We evaluate the mode h_{22} using the surrogate model described in Sec. II B. We will call the waveform computed via this procedure the "quadrupole" model.

b. Minimal waveform model.—Favata also constructed what he called the "minimal waveform model" (MWM) in [21]. The MWM is an analytical approximation to the time-domain quadrupole GW memory waveform, which is based on using the PN approximation to the waveform during the inspiral and a superposition of quasinormal modes during the merger and ringdown. It was then calibrated (by a constant rescaling) to match with the memory computed from an early effective-one-body (EOB)

waveform model tuned to NR simulations [58]. The time-domain MWM also has a Fourier transform that can be computed analytically to give an analytic frequency-domain waveform for the GW memory effect. This allows the MWM to be computed rapidly, which has made it useful in studies that perform Bayesian inference using GW memory models (e.g., [31,59]). However, the EOB model [58] against which the MWM was calibrated was not as precisely tuned to NR, and it overestimates the amplitude of the GW memory effect (this was noted in [21] and also in [35]). Nevertheless, because the MWM is a common approximation, we include it as the second of our three approximate methods.

c. Quadrupole and higher multipole model.—The waveform from the GW memory effect had been computed to 3PN order in [15], and at this order in the PN approximation, subdominant modes of the oscillatory GW strain enter into Eq. (2.9). The PN approximation only holds during the inspiral of a BBH, so it was only more recently in Talbot *et al.* [35] that higher multipole moments were included for the full inspiral-merger-ringdown waveforms used to calculate the GW memory. Specifically, in [35], higher-order GW modes up to (and including) $\ell = 4$ were used in Eq. (2.9) to compute $h_+^{\rm mem} - ih_\times^{\rm mem}$. Including the higher-order modes resulted in a roughly ten-percent increase in the amplitude of the GW memory effect, for comparable mass binaries. Accompanying the paper [35] was the release of a Python package called GWMEMORY [60]. We compute the GW memory waveform using this package with the oscillatory GW modes generated by the surrogate waveform model in Sec. II B (we leave out the h_{55} mode, because the GWMEMORY package does not compute the angular integrals for oscillatory modes with $l \geq 5$). We will refer to this third memory waveform model as the "higher-mode" model.

2. Illustration of differences between waveform models

We now show the differences that arise from using the different prescriptions for the three gravitational waveform models of the GW memory effect for a typical stellar-mass BBH system. Figure 1 shows $h_+^{\rm mem}(t)$ (top panel) and $|\tilde{h}_+^{\rm mem}(f)|$ (bottom panel) for the three GW-memory waveform models for a BBH with masses $m_1 = 30M_\odot$ and $m_2 = 30M_\odot$. We choose the luminosity distance to be $d_L = 500$ Mpc and the inclination angle to be $\iota = \pi/2$ (we replace r with d_L for binaries at cosmological distances). We set the value of $h_+^{\rm mem}(t)$ to be zero at the starting time in the top panel of Fig. 1, for this comparison.[5] We compute the Fourier transform $\tilde{h}_+^{\rm mem}(f)$ from $h_+^{\rm mem}(t)$ in the following ways: For the MWM, we use the analytical expression given in [21]; for the other two models, we pad the time domain waveform, window the time-domain waveform with a Planck window [61] to remove edge effects, and use the fast Fourier transform (FFT) algorithm [62] implemented in NUMPY [63,64].

While the time dependence of the three models is similar, the amplitudes are not. The quadrupole and higher-mode models are similar [they differ in the constant value of $h_+^{\rm mem}(t)$ at late times t by around ten percent]. These two models, however, differ from the MWM by a larger amount. This difference is also present in the frequency domain waveforms, although it is more difficult to observe in the bottom panel of Fig. 1.

The higher-mode model of [35] is expected to be the most accurate of the three, because it introduces the fewest assumptions and approximations. However, it is also the slowest to compute, because it involves the largest number of waveform modes. Because the quadrupole approximation of [21] differs by a relatively small amount and is faster to compute, we will use this waveform for most of our forecasts in Sec. IV; however, this will slightly underestimate the signal to noise of the memory effect in the population of BBHs. The MWM would typically overestimate it instead (we describe this in more detail in Sec. IV B).

E. Degeneracies between waveform parameters

We discuss in this section properties of the quantities $h_{(lm)}(t)$ introduced in Eq. (2.4) that will affect whether a given detection will be likely to contribute any significant evidence for the GW memory in the population of binaries (similarly to what was done in [31]).

In GW parameter estimation, it is well known that there are strong correlations between some parameters measured from a BBH merger by interferometric detectors when performing parameter estimation using just the dominant $l = 2$, $m = 2$ waveform mode (e.g., the correlation between inclination ι and luminosity distance d_L [65]). It is also well known, however, that by including higher-order modes in the waveform model, some of these correlations can be broken and improved constraints on the parameters of the gravitational waveform model can be obtained [66–70].

One salient type of correlation for detecting the GW memory effect was noted by Lasky *et al.* in [31]: namely, they described a degeneracy for the dominant $l = 2, m = 2$ under transformations of the form

$$(\psi, \phi_c) \to (\psi', \phi_c') = (\psi + \pi/2, \phi_c + \pi/2). \tag{2.12}$$

The quantity $h_{(22)}(t)$ was invariant, but other modes $h_{(lm)}(t)$ were not. The reason for the degeneracy of $h_{(22)}(t)$ is straightforward to understand: At fixed sky location (α, δ), the antenna patterns F_+ and $F_\times$ are periodic in the polarization angle $\psi \in (0, \pi)$; thus, the transformation $\psi \to \psi + \pi/2$ changes the sign of the antenna patterns

[5]The MWM includes an initial offset from zero that is computed from the PN approximation, while the other models do not.

$F_+ \to -F_+$ and $F_\times \to -F_\times$. Because the polarizations associated with the mode h_{22} satisfy $h_+^{22} - ih_\times^{22} \propto e^{2i\phi_c}$, then under the transformation $\phi_c \to \phi_c + \pi/2$ it follows that $h_+^{22} - ih_\times^{22} \to -(h_+^{22} - ih_\times^{22})$. This leaves the mode $h_{(22)}(t)$ invariant under this transformation.

For the purposes of discussing some of the correlations we have found in this work, it will be useful to consider the slightly more general transformation

$$(F_+, F_\times, \phi_c) \to (\pm F_+, \pm F_\times, \phi_c + \beta). \tag{2.13}$$

For a general mode $h_{(\ell m)}(t)$, a straightforward calculation then shows that under the transformation (2.13), the mode transforms as

$$h_{(\ell m)}(t) \to \pm[F_+ h_\times^{\ell m}(t) - F_\times h_+^{\ell m}(t)] \sin m\beta \pm h_{(\ell m)}(t) \cos m\beta. \tag{2.14}$$

The case $m = 2$, $\beta = \pi/2$, and the sign flip for F_+ and $F_\times$ recovers the degeneracy of the mode $h_{(22)}(t)$ discussed in detail above [and the expression above shows it is actually valid for any mode with $m = 2 \pmod 4$ and $\beta = \pi/2$].

We conclude this part by noting a few other degeneracies, and how these degeneracies can be broken. For example, the degeneracy of the mode $h_{(22)}(t)$ discussed above is not shared by a number of other modes. For example, when $m = 1$ or $m = 3 \pmod 4$ and $\beta = \pi/2$, then the $h_{(\ell m)}(t)$ transform in a nontrivial way under (2.13). Similarly, when $m = 0 \pmod 4$ and $\beta = \pi/2$, then the expression in Eq. (2.14) reduces to $h_{(\ell m)}(t) \to \pm h_{(\ell m)}(t)$. Thus, the presence of any of these higher-order modes $h_{(\ell m)}(t)$ in $h(t)$ (including the memory modes with $m = 0$) will break this degeneracy in Eq. (2.12). If $h(t)$ has as its dominant two modes $h_{(22)}(t)$ and $h_{(44)}(t)$, then the degeneracy in Eq. (2.12) will still be broken; however, there will be an additional degeneracy under the transformation that leaves F_+ and $F_\times$ invariant and has $\beta = \pi$ (this will be discussed further in Sec. IV A). Finally, it need not be simply the transformation $\psi \to \psi + \pi/2$ that changes the sign of the antenna patterns F_+ and $F_\times$. In Appendix C is an example of an unfortuitous sky location that leads to an additional degeneracy among the right ascension and declination.

III. METHODS FOR ASSESSING THE PRESENCE OF THE GW MEMORY EFFECT IN A BBH POPULATION

In this section, we discuss how we assess when the GW memory effect is present in a population of BBHs. Specifically, we describe computing signal-to-noise ratios (SNRs) for individual events and for populations of events, and determining a criteria like that used in [31] for when a given event will contribute significant SNRs towards finding the memory effect in the population of BBHs. In connection with this last point, we discuss Bayesian inference.

A. Computing signal-to-noise ratios

In the context of GW data analysis, matched filtering is an important component of finding and assessing the significance of a GW signal that is buried in what is generally assumed to be stationary Gaussian noise of a GW detector (see, e.g., [65,71]). The filter involves cross correlating the detector output $d(t) = s(t) + n(t)$ [where $s(t)$ is the GW signal and $n(t)$ is the detector noise] with a bank of template gravitational waveforms, $h(t)$. This cross correlation of the data and a template is most conveniently written in terms of the noise-weighted inner product in the frequency domain as

$$\langle d|h\rangle = 4\mathrm{Re}\int_{f_0}^{f_1} df \frac{\tilde{d}^*(f)\tilde{h}(f)}{S_n(f)}. \tag{3.1}$$

Here $\tilde{d}(f)$ and $\tilde{h}(f)$ are the Fourier transforms of the $d(t)$ and $h(t)$, respectively, and $S_n(f)$ is the one-sided power spectral density (PSD) of the detector's noise. The frequencies f_0 and f_1 define, respectively, the lower and upper range of the detector's sensitivity in the frequency domain. The inner product of the signal with itself is the square of the optimal signal-to-noise ratio (SNR):

$$\rho^2 = \langle s|s\rangle. \tag{3.2}$$

Equations (3.1) and (3.2) are important elements in assessing the likelihood of a signal existing in noisy data (see, e.g., [71] for more detail).

The signal $s(t)$ is generally not known *a priori*, so in practice, the square of the SNR is estimated from the data by computing the inner product of the data $d(t)$ with a family of templates $h(t;\vec{\theta})$ with different parameters $\vec{\theta}$. If Bayesian parameter estimation is used to construct a posterior probability distribution $p(\theta|d)$ for the parameters $\vec{\theta}$, then in general, there will be a distribution of squared matched filter SNRs, which can be computed from

$$\rho^2(\vec{\theta}; d) = \langle d|h(\vec{\theta})\rangle, \tag{3.3}$$

where $h(\vec{\theta})$ are the template waveforms that are consistent with the parameters $\vec{\theta}$ of the posterior probability distribution. For a single noise realization, the median of this distribution will not necessarily equal the optimal SNR given by $\sqrt{\langle s|s\rangle}$. However, for an event with a high SNR in Gaussian noise, the expected value of this median will be the optimal SNR, when averaging over different noise realizations. This will not necessarily be the case for signals with low SNRs or signals that transform nontrivially under some of the degeneracies discussed in Sec. II E (as we will discuss in more detail in Sec. IV A).

In this paper, we will compute a number of SNRs. For individual events in a single GW detector these SNRs are as follows: (i) the SNR $\rho_i^{\rm osc}$, which corresponds to the SNR for the ith GW detector (LIGO Hanford, LIGO Livingston, or Virgo) from the oscillatory GW modes for a BBH described in Sec. II B; (ii) the SNR ρ_i^{22}, which is the SNR of just the dominant $\ell = 2$, $m = 2$ mode; (iii) the SNR $\rho_i^{\rm hom}$, which contains all the oscillatory modes except for h_{22} and h_{32}; and (iv) the SNR $\rho_i^{\rm mem}$, which is the SNR for the GW memory signals described in Sec. II D. For signals that are measured in N_d detectors (where $N_d = 3$ in this paper), the network SNR is typically taken to be the sum in quadrature of the individual detector SNRs for each relevant class of signal:

$$\rho_N^2 = \sum_{\rm i=1}^{N_d} \rho_{\rm i}^2. \tag{3.4}$$

This is a reasonable definition when the Gaussian noise in each detector is independent of the other detectors.

As a practical matter, we compute the SNRs for all the different types of GW signals as follows. If the signal is not already in the frequency domain, we take the time-domain signal and apply a Planck window [61] before computing the Fourier transform. The upper limit of the relevant integral is taken to be the Nyquist frequency, (i.e., half of our sampling frequency $f_s = 8192$ Hz). The lower limit is chosen to be $f_0 = 10$ Hz, which is the low-frequency cutoff of the noise curves that we use for the PSDs of the Advanced LIGO and Virgo detectors. Specifically, we use the PSDs for aLIGO and Virgo at their design sensitivities, which are given in [72,73].

B. The case for combining subthreshold GW-memory-effect signals

For nonprecessing BBH mergers, there is a clear hierarchy of SNRs for the dominant, higher-order, and memory modes of the waveform (i.e., $\rho_N^{22} > \rho_N^{\rm hom} > \rho_N^{\rm mem}$).[6] As a rough rule of thumb, when the SNR of a particular signal is less than around 1, that signal is sufficiently weak that neither can it be claimed to be detected, nor can much be inferred about it from the data. More concretely, if, for example, $\rho_N^{\rm osc}$ exceeds the threshold of detection, but $\rho_N^{\rm mem}$ is less than 1, then neither would it be possible to claim detection for the memory effect nor would including the memory effect in waveforms used for parameter estimation inform the posterior distributions for the parameters in the waveform model. At the same time, when there is a confident detection of the dominant mode h_{22}, but the SNR for the higher-order modes does not itself pass the SNR threshold, the higher-order modes may still influence the estimation of parameters if $\rho_N^{\rm hom}$ is still greater than around 1. This last point has important implications for detecting the GW memory effect, which were noted in [31], because the higher-order modes turn out to be useful for breaking some of the degeneracies mentioned in Sec. II E.

Given what is currently known about the population of BBHs from the LIGO and Virgo observations [32], the sensitivities of the Advanced LIGO and Virgo detectors, and the relative strengths of the dominant, higher-order, and memory modes, it is expected that the detected events will fall into the following classes of SNRs for the different modes: (i) a significant fraction of the events will have ρ_N^{22} passing the threshold for detection, $\rho_N^{\rm hom} < 2$, and $\rho_N^{\rm mem} < 1$; (ii) a smaller fraction of events will have ρ_N^{22} passing the threshold for detection, $\rho_N^{\rm hom} > 2$ but under the threshold of detection, and $\rho_N^{\rm mem} < 1$; and (iii) a handful of events with ρ_N^{22} passing the threshold for detection, $\rho_N^{\rm hom} > 2$, and $\rho_N^{\rm mem} > 1$ (some of these events may have $\rho_N^{\rm hom}$ near the threshold for detection, but it is not expected that $\rho_N^{\rm mem}$ will reach this level). More detailed numbers for specific BBH populations are given in Sec. IV C.

Because there are expected to be a large number of detections of BBHs, and because the SNR of the memory effect is not expected to exceed the threshold for detection, it seems reasonable to follow the approach of Lasky *et al.* [31], who proposed combining multiple BBH detections with subthreshold memory signals to provide evidence for the effect in a population of BBH mergers. To assess whether the memory was present in the population, [31] uses two methods, one based on computing evidence ratios for signals with and without memory modes, and a second based on computing the SNR of the memory in the population of BBH events. We more closely follow the second approach of [31] based on the total SNR of N_e events measured in network of N_d detectors (though we briefly discuss the relationship between the two methods in Sec. V).

Assuming that all the events are independent, the noise in the network is Gaussian, and the signal in the data is known exactly, then the total SNR for the memory waveforms in the population of BBHs is given by

$$\rho_{\rm tot} = \sqrt{\sum_{\rm j=1}^{N_e} (\rho_{N,j}^{\rm mem})^2}. \tag{3.5}$$

Here $\rho_{N,j}^{\rm mem}$ is the network SNR of the GW memory effect in the detector network for the jth detection. The SNR in Eq. (3.5) will grow approximately with the number of detections and detectors as $\sqrt{N_e N_d}$.[7] If the memory signals for each event are known, then the quantity $\rho_{N,j}^{\rm mem}$ could be

[6] For example, for an event consistent with GW150914 [1,3,74], the SNRs are $\rho_N^{\rm osc} = 76.5$, $\rho_N^{22} = 75.9$, $\rho_N^{\rm hom} = 3.9$, and $\rho_N^{\rm mem} = 0.21$ (for the quadrupole memory waveform model).

[7] This growth is also explained in Appendix B, using an analogy based on stacking GW memory waveform signals.

computed from Eqs. (3.2) and (3.4). However, when the signal is not known *a priori*, one might instead consider using the median value of the SNR in Eq. (3.3) to determine the network SNR (3.4) of the memory effect for the jth detection.

Using the median value in Eq. (3.3) leads to certain complications, because of the hierarchy of SNRs described in this part and the degeneracies among the waveform parameters discussed in Sec. II E. Consider, for example, the case when ρ_N^{22} passes the threshold for detection, $\rho_N^{\rm hom} < 2$, and $\rho_N^{\rm mem} < 1$. Because of the degeneracies described in Sec. II E, then the SNRs for the parameters $\vec{\theta}$ and $\vec{\theta}'$ [defined by the transformation in Eq. (2.12)] will satisfy $\rho^2_{\rm mem}(\vec{\theta}';d) \approx -\rho^2_{\rm mem}(\vec{\theta};d)$. Thus, both sets of parameters will be nearly equally consistent with the observed data, and the distribution of matched-filter SNRs for the GW memory effect will contain significant support for both positive and negative values (so that the median would be close to zero). However, as Lasky *et al.* observed in [31], there could be a sufficient number of events with ρ_N^{22} passing the threshold for detection, $\rho_N^{\rm hom} > 2$ but under the threshold of detection, and $\rho_N^{\rm mem} < 1$. For these events, the higher-order modes can break the degeneracies that allow strains $h_{\rm mem}$ with opposite signs to be consistent with the data, so that the true value of the SNR will be close to the median value (this will also be shown in more detail in Sec. IV A).

Therefore, if one were to use all detected events, N_e, to estimate the total SNR for the memory effect in the population, $\rho_{\rm tot}$, in Eq. (3.5), this would generally overestimate the SNR, because of the degeneracies discussed in the previous paragraph. Instead, there are two approximations that one could make to obtain a more realistic estimate of the SNR $\rho_{\rm tot}$: The first would be to replace $\rho^{\rm mem}_{N,j}$ in Eq. (3.5) with the median value that is consistent with the posterior distribution of parameters of the waveform. We will *not* take this approach in this paper. Rather, we will instead follow a procedure like that in [31], in which we will only consider those events in which $\rho_N^{\rm hom}$ satisfies a SNR threshold cut (similarly to in [31], we choose this to be $\rho_N^{\rm hom} > 2$, for reasons which we discuss more in Sec. IV A). Thus, we will estimate the SNR of the memory effect in a BBH population by

$$\rho_{\rm tot} = \sqrt{\sum_{\rm j=1}^{N'_e} (\rho^{\rm mem}_{N,j})^2}, \tag{3.6}$$

where N'_e is the number of detected events that satisfy our SNR cut for the higher-order modes, and $(\rho^{\rm mem}_{N,j})^2$ is computed from Eqs. (3.2) and (3.4).

Note that choosing the hard cut of $\rho_N^{\rm hom} > 2$ may underestimate the total SNR of the memory effect, because some events near the threshold, but that do not make the cut, could still contribute a reduced, though nonzero, SNR. Thus, we will typically compute the SNR using both Eqs. (3.5) and (3.6) as ways of roughly estimating a lower and upper bound for the memory SNR. In the next part of this section, we discuss our choice for the SNR threshold in more detail, and the Bayesian methods that we used to determine this criteria.

C. Determining the "sign" of the memory effect through inference of the source parameters

In [31], Lasky *et al.* determined a criteria based on the SNR required in a particular combination of higher-order modes with $m = 1$ and $m = 3$ which broke the degeneracy in Eq. (2.12) for the mode $h_{(22)}$. In terms of the somewhat more general transformation in Eq. (2.13), the degeneracy we would like to break is that between the two signs of the antenna patterns $\pm F_+$ and $\pm F_\times$ for some of the specific angles β discussed in Sec. II E. The reason for this is as follows: In the quadrupole approximation the strain $h^{\rm mem}_+$ [computed from Eq. (2.11)] is non-negative and is independent of β; thus, the sign of memory strain measured by a GW detector, $h_{\rm mem}$, is completely determined by the sign of the antenna pattern F_+. We will sometimes then refer to the breaking of the degeneracy in Eq. (2.13) [or (2.12)] as determining the sign of the memory effect (or just "the memory sign"), as was done in [31]. Rather than using the specific combination of higher-order modes used in [31], we will base our criteria on the SNR $\rho_N^{\rm hom}$ [as we discussed in Sec. II E, other modes besides the $m = 1$ and $m = 3$ modes can break the degeneracy in Eq. (2.13) for particular values of β].

To determine whether we can measure the sign of the memory effect, therefore, we need to determine how accurately we can measure the four parameters that determine the degeneracy in Eq. (2.13): right ascension α, declination δ, polarization ψ, and phase ϕ_c. For most sufficiently well localized sources at most sky locations, this degeneracy reduces to resolving the degeneracy between the latter two parameters ψ and ϕ_c.

To ascertain how well we can recover the unknown signal parameters, we use Bayesian inference [75–77] to compute posterior probability density functions (PDFs) for the relevant parameters. Specifically, given the detector output d and a signal hypothesis H that involves a set of parameters $\vec{\theta}$, we compute the posterior PDF for the parameters $\vec{\theta}$ via Bayes' theorem:

$$p(\vec{\theta}|d,H) \propto \mathcal{L}(d|\vec{\theta},H)p(\vec{\theta}|H). \tag{3.7}$$

Here $p(\vec{\theta}|H)$ is the prior PDF for the parameters $\vec{\theta}$ and $\mathcal{L}(d|\vec{\theta},H) = p(d|\vec{\theta},H)$ is the likelihood function. For our detector network, we assume that the noise is Gaussian and that the noise in each detector is uncorrelated with the other

detectors. This implies we can write the joint likelihood as the product of the individual likelihoods [65,77]:

$$\mathcal{L}_N = \prod_{i=1}^{N_d} \mathcal{L}_i(d_i|\vec{\theta}, H). \tag{3.8}$$

The log of the individual likelihoods of the data in each detector given some signal model $H \equiv h(\vec{\theta})$ is given by (see, e.g., [65])

$$\log \mathcal{L}(d|\vec{\theta}, H) \propto -\frac{1}{2}\sum_{i=1}^{N_d} \langle d_i - h_i(\vec{\theta})|d_i - h_i(\vec{\theta})\rangle. \tag{3.9}$$

For a BBH in a quasicircular orbit, there are 15 parameters in $\vec{\theta}$. We will restrict to nonspinning binaries for our parameter estimation studies, which reduces the dimension of the parameter space to nine. Because the degeneracy is among the extrinsic parameters and there generally are not strong correlations between intrinsic and extrinsic parameters [65], we fix the component masses of the binary to their true values. This leaves us with the extrinsic parameters, given by the set $\vec{\theta} = \{d_L, \iota, \alpha, \delta, \psi, \phi_c, t_c\}$. The last parameter t_c, which had not been introduced previously, is the time at coalescence. For each of these extrinsic parameters we specify the prior PDFs to be uninformative priors. Specifically, we take the priors for the source's sky location to be isotropic and the luminosity distance to be uniform in volume. The width of the distance prior is adjusted to cover a sufficiently large range around the true luminosity distance of the binary. For the prior on the orientation of the binary with respect to the line of sight, we again assume an isotropic prior. Finally, we take the priors for the polarization to be uniform in $(0, \pi)$ and for the coalescence time t_c to be uniform in a 200 ms window centered on the true value.

Although, in general, the detector output consists of both the GW strain and a realization of Gaussian noise, for our parameter estimation studies, we do not include any noise. The intent of this approximation is to better understand the correlations and degeneracies among parameters as a function of $\rho_N^{\rm hom}$ without introducing a bias from a specific noise realization (though with noise, one may sometimes require a higher value of $\rho_N^{\rm hom}$ to break the degeneracies). The results we find without noise also should be similar to those that would be obtained from averaging over many random Gaussian noise realizations with zero mean. The detector noise is taken into account when calculating the noise-weighted inner product in Eq. (3.9), because it involves the noise power spectral density of the GW detectors.

We use the ensemble MCMC sampler KOMBINE [78] to determine the posterior PDF from Eq. (3.7) for detector data consisting of the waveform from a binary with parameters $\vec{\theta}_{\rm true}$. From the posterior PDF, we can determine if the degeneracy between ψ and ϕ_c is broken (i.e., if the PDFs of these angles will be concentrated around the true values) or not (i.e., there is similar support in the posterior PDFs for ψ and ϕ_c and both values shifted by $\pi/2$). This will determine how conclusively we can measure the sign of the memory for this particular binary. With the posterior PDFs, we can then also compute for each point $\vec{\theta}_s$ in the parameter space the associated GW memory waveform $h_{\rm mem}(\vec{\theta}_s)$ using the quadrupole model, and the corresponding estimate for the square of the SNR in Eq. (3.3). We will discuss the results of these calculations in the next section.

IV. RESULTS: MEMORY SIGN AND FORECASTS FOR DETECTION OF THE GW MEMORY EFFECT

In the first part of this section, we illustrate how the presence of higher-order GW modes allows the sign of the GW memory effect to be measured. In the next two sections, we highlight the number of detections and the amount of detector time necessary to detect the GW memory effect in several different types of populations of BBHs. We first consider a BBH population of GW150914-like events followed by two classes of BBH populations that are consistent with the models of the BBH populations computed by the LIGO and Virgo collaborations in [32].

A. Measuring the memory sign

In principle, it would be possible to perform Bayesian inference on every binary in a population of BBHs, to determine whether we can confidently determine the median network SNR of each GW memory effect in the data. Because of the significant computational cost of doing this, similarly to in [31], we instead look for a criteria based on $\rho_N^{\rm hom}$ that will be satisfied when we confidently know the sign of the memory, which we can then use in lieu of full Bayesian parameter estimation. To establish this criterion, we perform Bayesian inference on a handful of BBHs of different masses, sky locations, polarizations, and orientations of the binaries. A representative result for an equal mass BBH is shown in Fig. 2. We use this result to demonstrate that the criteria of $\rho_N^{\rm hom} > 2$ will be sufficient for most BBHs. However, we caution that there can be small regions of the extrinsic parameter space where this criteria is not as strong, for particular sky locations. One such example is shown for a BBH with $q = 3/2$ in Appendix C.

For each binary, we tune the amplitude of $\rho_N^{\rm hom}$ either by changing the luminosity distance d_L or the inclination ι (in the former approach, all the SNRs of the different modes scale inversely with the distance in the same way, whereas in the latter approach, the relative amplitudes of the SNRs of the different modes change much more). We run Bayesian parameter estimation, as described in

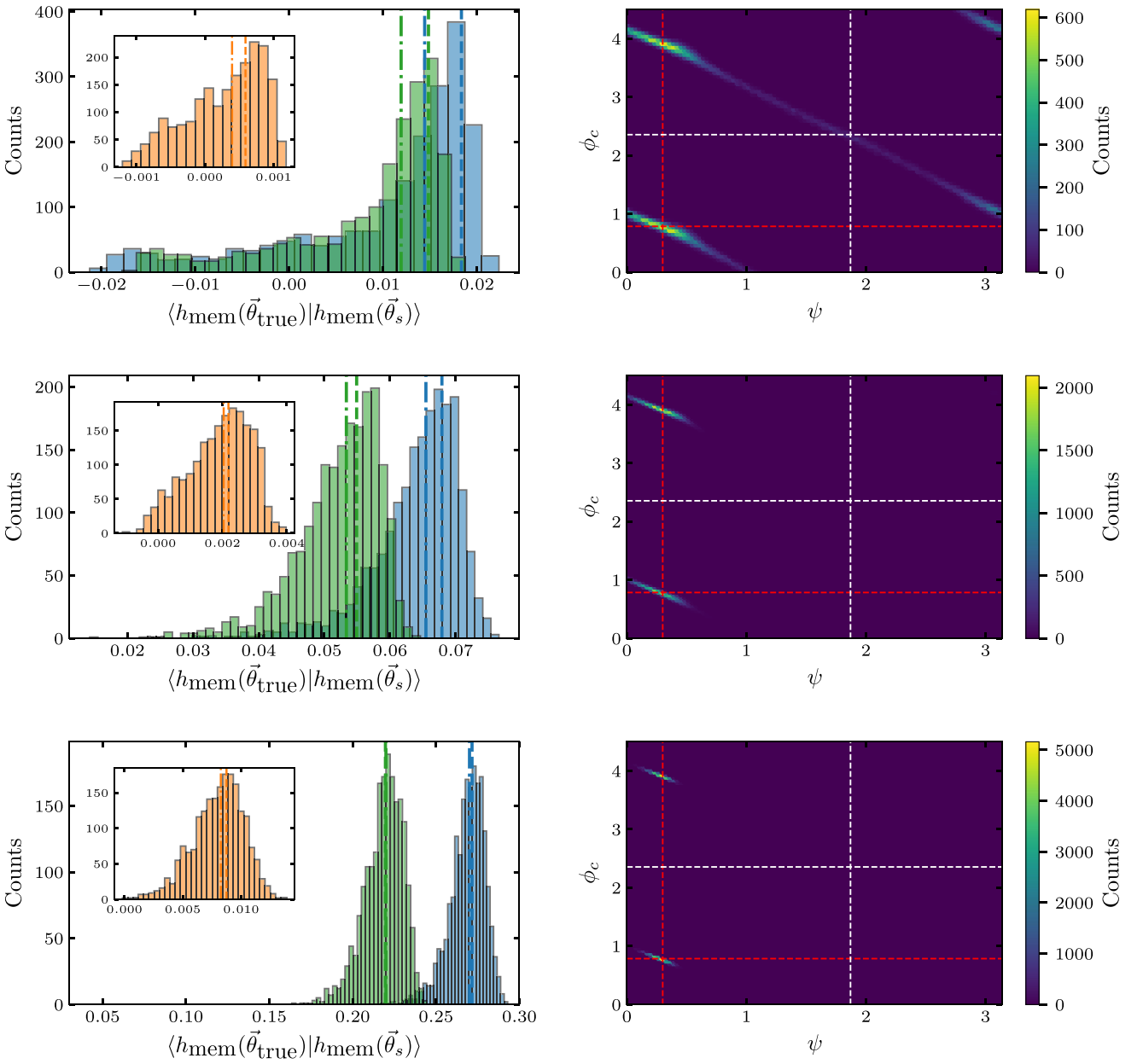

FIG. 2. Posterior distributions (not normalized) for a nonspinning, equal-mass binary with $m_1 = m_2 = 30M_\odot$ with extrinsic parameters given by $\alpha = 4.2$ rad, $\delta = -0.8$ rad, $\psi = 0.3$ rad and $\iota = 2.1$ rad. Left column: The overlap between the true signal, $h_{\rm mem}(\vec{\theta}_{\rm true})$, and templates consistent with the posteriors, $h_{\rm mem}(\vec{\theta}_s)$, for three different SNRs in the higher-order modes, $\rho_N^{\rm hom}$. From top to bottom the SNRs are $\rho_N^{\rm hom} \approx 1$, 2, and 4; the different SNRs were obtained by varying the luminosity distance of the source, while keeping other parameters fixed. The inner product for Advanced LIGO Hanford, LIGO Livingston and Virgo are shown in green, blue, and orange, respectively. The vertical dashed lines represent the optimal ρ^2 injected values and the vertical dot-dashed lines represent the median values of the distributions. Right column: The 2D PDFs for ψ and ϕ_c, for the same binaries in the corresponding rows. Red dashed lines show the "true" injected values and the white dashed line shows the degenerate values. Already at an SNR of 1, the ψ-ϕ_c degeneracy is partially broken, whereas for the SNRs 2 and 4 in the middle and bottom rows, the degeneracy is broken, and the sign of the detector's response to the memory effect is well known for all detectors.

Sec. III C, to determine how large $\rho_N^{\rm hom}$ must be to break the degeneracies and to determine the sign of the GW memory effect.

We show the results for an equal mass BBH with $m_1 = m_2 = 30M_\odot$ in Fig. 2. The three rows correspond to three luminosity distances $d_L = 1250$, 650, and 325 Mpc (going from top to bottom); the corresponding SNRs $\rho_N^{\rm hom}$ are given by $\rho_N^{\rm hom} \approx 1$, 2 and 4, respectively. This binary is detectable by the advanced detector network at all three distances, because the oscillatory SNRs are roughly 25, 48

and 96. The left column shows the inner product of the data [the true signal $h_{\rm mem}(\vec{\theta}_{\rm true})$] with templates that are consistent with the posteriors, $h_{\rm mem}(\vec{\theta}_{\rm s})$. The blue and green histograms correspond to this inner product for the Advanced LIGO Livingston and Hanford, respectively, and the inset orange histogram shows this for the Virgo detector. The right column shows the 2D posterior PDF for the parameters ψ and ϕ_c.

When $\rho_N^{\rm hom} \approx 1$, we find that the degeneracy in Eq. (2.12) between ψ and ϕ_c is not fully broken; thus, there is nontrivial support for both signs of noise-weighted inner product $\langle h_{\rm mem}(\vec{\theta}_{\rm true})|h_{\rm mem}(\vec{\theta}_{\rm s})\rangle$ in the left panel. This occurs because although the true values of ψ and ϕ_c are favored (indicated by the intersection of the red dashed lines), there is also some support for the true values both shifted by $\pi/2$ (indicated by the intersection of the white dashed lines). The presence of the negative noise-weighted inner product is most obvious for Virgo (in the inset), where the amplitude of the inner product is smallest; however, it is also visible in the histograms for LIGO-Hanford and LIGO-Livingston, despite the larger amplitude for the inner product.

For $\rho_N^{\rm hom} \approx 2$, almost all templates $h_{\rm mem}(\vec{\theta}_s)$ consistent with the posterior PDFs have the correct sign, which occurs because the degeneracy of Eq. (2.12) is now almost fully broken. For $\rho_N^{\rm hom} \approx 4$, ψ and ϕ_c are even better constrained, and the overlap for all detectors is closely centered around the optimal SNR squared. Note that there is a remaining degeneracy between ϕ_c and $\phi_c + \pi$ apparent in the 2D posteriors even at the large values of $\rho_N^{\rm hom}$. This occurs because the majority of the SNR in $\rho_N^{\rm hom}$ comes from $h_{(44)}$ (this was noted in Sec. II E). This residual degeneracy does *not* affect the sign of the GW memory effect, however.

The results in Fig. 2 are representative of the required network SNR in the higher-order modes, $\rho_N^{\rm hom}$, that is needed to break the degeneracies that determine the sign of the memory in at least one detector (though see Appendix C for an example of a very specific sky location and polarization that requires a slightly higher value of $\rho_N^{\rm hom}$). Thus, we conclude that binaries for which the network SNR $\rho_N^{\rm hom} \geq 2$ is sufficient to be able to determine the memory sign. As a result, we will use this criteria to determine when we include a given detection in the total SNR for the memory in Eq. (3.6) in a BBH population. This criteria is used throughout the next two subsections.

B. GW150914-like binary-black-hole population

Before we investigate different populations from those studied in [31], we first aim to understand the effects of using a different waveform model and a slightly different criteria for the SNR in the higher-order GW modes on the same population of BBHs used by [31]. Specifically, we consider in this section a population of GW150914-like binaries. These are nonspinning binaries with $m_1 = 36M_\odot$, $m_2 = 29M_\odot$ and $d_L = 410$ Mpc, which are values consistent with GW150914 [74]. The rest of the binary's parameters are distributed uniformly in α, $\sin\delta$, $\cos\iota$, ψ and ϕ_c. In this analysis, as in Ref. [31], we use a detector network of the two LIGO detectors at design sensitivity [72], and we use a network SNR for the oscillatory part of the signal of 12 as our threshold for detection (i.e., $\rho_N^{\rm osc} \geq 12$).

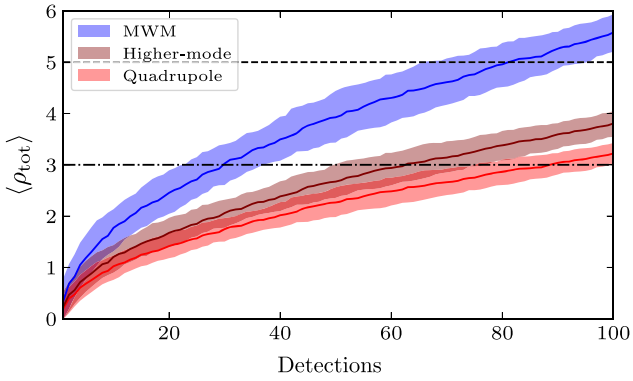

FIG. 3. The total memory SNR versus the detection number for a population of GW150914-like binaries computed with the three GW memory waveform models in Sec. II D. The solid lines are the median values over 100 realizations of this population, and the shaded regions are 1-σ confidence intervals. The colors red, maroon, and blue correspond to the quadrupole, higher-mode, and MWM models, respectively. The dot-dashed and dashed black lines show two SNR thresholds used in [31]. Our calculations with the MWM are consistent with the ones in [31] (which also used the MWM). The other two models have notably smaller SNRs for the memory effect.

We calculate the GW memory waveforms for all detections using the three different waveform models described in Sec. II D. For each model, we calculate the associated total memory SNR from Eq. (3.5) for a population of 100 GW150914-like binaries. For detections with $\rho_N^{\rm hom} \geq 2$ (where just higher-order modes with $l \leq 3$ and odd $|m|$ are used), we include the network SNR for the memory effect in the sum, and for the remaining detections, we set $\rho_{N,j}^{\rm mem} = 0$, for each of the waveform models (as was described in Sec. IV A).[8]

We repeat the above analysis for 100 realizations of this GW150914-like population (and we use the same realizations for the three different waveform models). Figure 3 shows how the total SNR for the memory effect grows over the 100 detections. The solid lines show the median SNR over the 100 realizations of the population, $\langle\rho_{\rm tot}\rangle$, and the shaded regions indicate the 1-σ confidence intervals (i.e.,

[8]Although we do not include GW modes $l > 3$ in the oscillatory waveform to match with [31], the higher-mode memory waveform is calculated using all modes up to $l = 4$ as stated in Sec. II D.

TABLE I. Total memory SNR $\langle\rho_{\rm tot}\rangle$ for the three different waveform models of Sec. II D after 30 and 90 detections. The numbers are the median value, and the error bars are 1-σ confidence intervals.

Detection number	MWM	Higher mode	Quadrupole
30	$3.10^{+0.33}_{-0.41}$	$2.11^{+0.23}_{-0.28}$	$1.79^{+0.19}_{-0.23}$
90	$5.30^{+0.36}_{-0.36}$	$3.61^{+0.24}_{-0.25}$	$3.06^{+0.21}_{-0.21}$

the symmetric, 68% credible region). The three colors (blue, maroon, and red) correspond to the three different waveform models described in Sec. II D (the MWM, higher-mode, and quadrupole, respectively).

For reference, we give the median value of the SNR $\langle\rho_{\rm tot}\rangle$ and the 1-σ confidence intervals for the population after 30 and 90 detections in Table I. We choose these numbers, because they are round numbers where the median value of $\rho_{\rm tot}$ for the MWM (the model used in [31]) is close to the two values of 3 and 5 used for the thresholds of detection in [31] (which are intended to represent 3- and 5-σ significant detections of the memory effect in the GW150914-like population). Our results for the MWM are similar to those found in [31]. As Table I shows, the higher-mode and quadrupole models (which make fewer assumptions when computing the GW memory effect) produce significantly smaller values for the total memory SNR in the GW150914-like population. We consider the results of these models to be more representative of the GW memory signal (for the reasons discussed in Sec. II D), so we expect the total SNR of the memory in this population of BBHs to be closer to these values.

We conclude this part by noting that for this GW150914-like population, on average two-thirds of the detections pass the SNR threshold in the higher-order modes.

C. Power-law mass-function populations

Nine additional BBHs were detected by the LIGO-Virgo collaboration after GW150914, in the first two observing runs, and these nine detections informed models of the population of BBHs [32]. We now repeat our calculations of $\langle\rho_{\rm tot}\rangle$ for populations that are consistent with the models in [32].

1. Simulated BBH populations

Specifically, we use model A of [32] for the distribution of the BH masses in a BBH system. For this model, the mass ratio of the binary q is assumed to follow a uniform distribution; the distribution of the primary component mass, m_1, is taken to be a power law (with index $\alpha_{\rm pow}$) and the mass range is restricted between $m_{\rm min}$ and $m_{\rm max}$. This means that the mass distribution can be written in the form

$$p(m_1, m_2|m_{\rm min}, m_{\rm max}, \alpha_{\rm pow}) = C(m_1) m_1^{-\alpha_{\rm pow}}, \qquad (4.1)$$

for $m_{\rm min} \leq m_2 \leq m_1 \leq m_{\rm max}$ [where $C(m_1)$ is the normalization] and the probability is zero outside this mass range. The minimum black hole mass $m_{\rm min}$ is fixed to be $5.0M_\odot$, so there are two free parameters in the mass distribution: $m_{\rm max}$ and $\alpha_{\rm pow}$. The parameters α_{pow} and $m_{\rm max}$ were inferred in [32] by assuming that the GW detections in the first and second observing runs followed a Poisson process with an unknown rate per comoving volume of BBH mergers, R. The three parameters were jointly inferred from the GW detections using Bayesian techniques. The median values of the mass-distribution parameters are $\alpha_{\rm pow} = 0.4$ and $m_{\rm max} = 41.6M_\odot$, while the rate per volume's median value is $R = 64.9\ {\rm Gpc}^{-3}\,{\rm yr}^{-1}$. These three parameters are correlated in nontrivial ways; see [32] for more detail.

We also allow the BHs in our population to have aligned spins. We again use the results of [32] to determine the distribution of spin parameters. Specifically, we assume that the aligned-spin magnitudes of each BH in the binary are independent of one another, and we assume that they follow the nonparametric binned distribution illustrated in the bottom panel of Fig. 7 of [32]. This model favors small aligned spins, so we do not expect the results to differ much from a population of nonspinning BBHs.

Because the surrogate model is valid for a subset of the allowed mass ratios and spins, we restrict to aligned-spin binaries with mass ratios $1 \leq q \leq 8$ and dimensionless spin magnitudes $|\chi_{1z}|$, $|\chi_{1z}| \leq 0.8$. We generate BBH mergers uniformly in comoving volume up to $d_L = 2$ Gpc (we do not observe a significant change in the total memory SNR by increasing d_L). The remaining extrinsic parameters of the binary are distributed in the same way as they were for the BBH population in Sec. IV B.

Because of the large range of masses and distances for the binaries in this BBH population, a more significant number of the simulated BBHs will not reach the SNR threshold for detection. We select the criteria for detection as follows: For the detector network, we choose the two Advanced LIGO detectors and the Virgo detector at their design sensitivities [72,73]. We consider a BBH merger to be detected if the three-detector network SNR satisfies $\rho_N^{\rm osc} \geq 8$ and if the single-detector SNRs satisfy $\rho^{\rm osc} \geq 4.5$ for LIGO and $\rho^{\rm osc} \geq 3.0$ for Virgo. To determine binaries for which we know the memory effect's sign, we use the criteria $\rho_N^{\rm hom} \geq 2$, as in Sec. IV B, although we now use all modes mentioned in Sec. II B except for the $l = 3$, $m = 2$ mode which does not break the degeneracies mentioned in Sec. II E.

The LIGO and Virgo detector network is not operational for all times, but just for a fraction of the time (which gets called the network's "duty cycle"). We therefore keep only the fraction of the detections consistent with the duty cycle of the three-detector network, which based on [79] is 50% (i.e., we exclude 50% of the binaries that make the SNR cut for detection). We calculate the total memory SNR for the

population in two ways. As a more conservative estimate, we use Eq. (3.6) to compute the SNR from the binaries that pass all three detection, duty-cycle, and higher-mode-SNR cuts. As an upper bound, we also calculate the total memory SNR in the same way except that we include the binaries that do *not* pass the higher-mode-SNR cut (this was also done in [31]). To determine the uncertainty arising from different realizations of the population, we generate 300 realizations, and we compute the median values and confidence intervals for the SNR over these different realizations. We use the quadrupole memory waveform model to model the memory effect in these simulated populations.

We simulate each realization for an observation period of five years; with the assumed duty cycle, this corresponds to 2.5 years of coincident data for the three-detector network. We find it more useful to compute the total SNR of the memory effect as a function of observation time, because both the number of detections and the types of detected binaries will vary over different realizations of the population, even for fixed values of the parameters $\alpha_{\rm pow}$, $m_{\rm max}$, and R.

We perform two types of analyses with the BBH population based on model A, which differ only in how we treat the parameters $\alpha_{\rm pow}$, $m_{\rm max}$, and R. First, we fix the parameters $\alpha_{\rm pow}$, $m_{\rm max}$, and R to their median values and sample the masses from 300 different realizations of populations with these median parameters. This highlights the uncertainty from different realizations of a fixed population. However, there are also uncertainties on the merger rate, the maximum mass, and the power law index. Thus, for our second analysis, we let the values of $\alpha_{\rm pow}$, $m_{\rm max}$ and R be drawn randomly from their respective posterior distributions given in [32]. This allows us to understand how the total GW memory SNR varies because of the uncertainty in the three parameters $\alpha_{\rm pow}$, $m_{\rm max}$, and R.

2. SNR for the GW memory effect

Figure 4 shows the total memory SNR gained versus detector operation time in years. The shaded regions indicate the 1-σ confidence intervals and the solid lines show the median SNR $\langle\rho_{\rm tot}\rangle$ for 300 realizations. The top panel of Fig. 4 shows the results from fixing R, $\alpha_{\rm pow}$, $m_{\rm max}$ to their median values. The bottom panel of Fig. 4 is the same as the top, except now R, $\alpha_{\rm pow}$ and $m_{\rm max}$ are allowed to vary. We give the median value of the SNR $\langle\rho_{\rm tot}\rangle$ and the 1-σ confidence intervals for both analyses after five years in Table II.

Figure 4 and Table II show that after five years of detector operation time, the total SNR for the GW memory in the population is approaching the SNR threshold of 3. Specifically, this threshold is close to the upper limit of the 1-σ confidence interval for the conservative estimate (the red region) and the lower limit of the confidence interval for the upper bound (the purple region). The SNR for the memory effect does not differ greatly between the populations with fixed and with varied parameters; the only obvious difference is a somewhat greater width of the 1-σ confidence intervals when the population parameters are varied. This is not surprising, because the fixed population

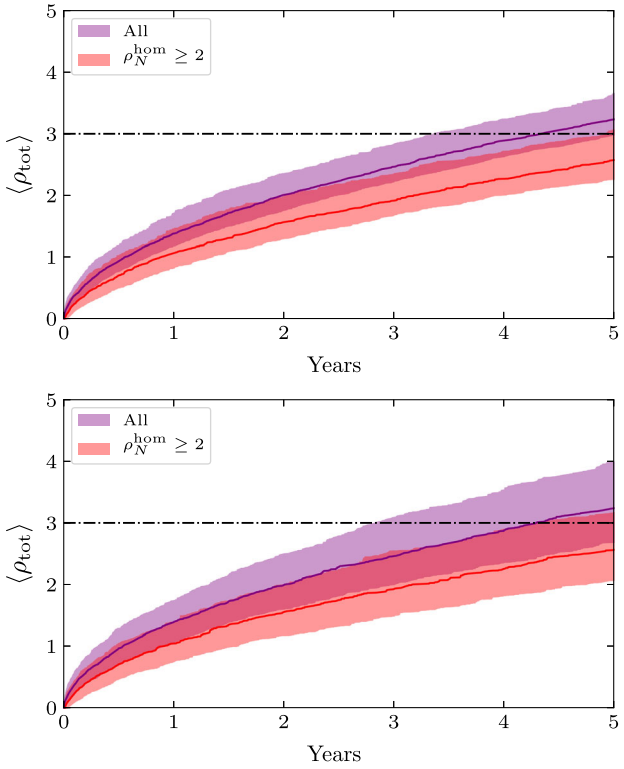

FIG. 4. The total memory SNR for two populations of BBHs generated using model A of [32] (see the text of Sec. IV C for further details). The memory SNR is calculated using the quadrupole memory model. The shaded regions indicate the 1-σ confidence intervals and the solid lines show the median SNR $\langle\rho_{\rm tot}\rangle$. In red, only the detections are included which pass our higher-mode-SNR cut $\rho_N^{\rm hom} \geq 2$. In purple, all detections are included. Top: The population parameters R, $\alpha_{\rm pow}$, and $m_{\rm max}$ are fixed to their median values. Bottom: R, $\alpha_{\rm pow}$ and $m_{\rm max}$ are drawn according to the distributions given in [32]. In both analyses, top and bottom panels, the GW memory effect is on the verge of being detected after five years of operation of the Advanced LIGO and Virgo detector network at design sensitivity.

TABLE II. Total memory SNR $\langle\rho_{\rm tot}\rangle$ for the two different analyses of Sec. IV C after five years of detector operation time. The numbers are the median value, and the error bars are 1-σ confidence intervals.

Population A	$\rho_N^{\rm hom} \geq 2$	All
Fixed	$2.58^{+0.50}_{-0.32}$	$3.24^{+0.42}_{-0.26}$
Varied	$2.57^{+0.61}_{-0.50}$	$3.24^{+0.75}_{-0.56}$

TABLE III. Percentages of detections that satisfy the given criteria for the SNRs for the higher-order modes and for the memory effect for individual detections. The criteria are given for both the fixed and varied populations discussed in Sec. IV C.

	$\rho_N^{\rm hom} < 2$	$\rho_N^{\rm hom} \geq 2$	$\rho_N^{\rm hom} \geq 2$
Population A	$\rho_N^{\rm mem} < 1$	$\rho_N^{\rm mem} < 1$	$\rho_N^{\rm mem} \geq 1$
Fixed	69.5%	30.4%	0.1%
Varied	70.4%	29.5%	0.1%

does not incorporate uncertainties on the rate, the maximum mass, and the power law, whereas the varied population does.

Because the results with and without the SNR cut for the higher order modes are not very different, it is of interest to know what fraction of the events pass this cut. This is highlighted in Table III. It shows that the majority of the events (around 70%) do not pass this cut. Thus, despite the large number of these events, their SNR is generally sufficiently small that they do not make a substantial difference to the total SNR for the memory effect. Table III also shows that it will be unlikely for a given realization of a population to have an event in the population that has $\rho_N^{\rm mem} \geq 1$. Thus, the majority of the total SNR for the memory comes from the louder subset of events that satisfy the criteria $\rho_N^{\rm hom} \geq 2$ and $\rho_N^{\rm mem} < 1$. This also was noted in [31].

V. DISCUSSION

In this paper, we investigated the prospects for detecting the nonlinear GW memory effect by the Advanced LIGO and Virgo detectors in different populations of BBHs. We first noted that of three commonly used methods to compute the memory effect, two produced similar results, whereas the other one differed by a larger amount. The two methods that more closely agreed made fewer approximations to compute the GW memory waveforms, and thus seem to be the more reliable waveform models for computing the GW memory effect and performing estimates of when the memory effect will be detected.

We also revisited the criteria used in [31] for assessing when an individual event will provide useful evidence for the presence of the memory in the population. An important insight in [31] was that degeneracies in the GW mode h_{22} lead to the SNR of the memory effect being uncertain for a single detection. However, even if the SNR of the memory effect is small, as long as higher-order modes of the GWs are measurable for each individual BBH detection, then the event will be useful for contributing to the total SNR for the memory effect in the population. We performed Bayesian inference on several simulated BBH detections to find that on average, a network SNR of 2 in the higher-order modes is sufficient to determine the memory effect's sign (and thus its SNR for that event). This criterion was similar to the one used in [31], but it used a different subset and combination of the higher-order modes.

We then simulated two classes of populations of BBHs to determine when the memory effect would be present in these populations. We first looked at the population of GW150914-like BBHs that was considered in [31]. Our results were consistent with those in [31] when we used the same GW waveform model as in [31], but the SNR of the memory was notably smaller when computed with the more recent waveform models that make use of fewer approximations. We then investigated the SNR for the memory effect in the simplest model for the astrophysical population of BBHs that was inferred from the first ten GW detections of BBHs in [32]. We considered two cases of this model, one where the parameters of the mass distribution and the rate were fixed to the median values, and one where we considered different realizations of the mass distribution and rate. In both cases, the SNR for the memory in the population was near the threshold of detection after five years (SNR of 3), when using one of the more recent GW memory waveform models. The spread of SNRs over different realizations of the populations for the two cases was larger when the parameters were not fixed to their median values, though, as a result of taking into account the additional uncertainties on the parameters describing the population.

The data used to generate the figures in this paper are available here [80].

ACKNOWLEDGMENTS

We thank Yanbei Chen and Samaya Nissanke for their input in the early stages of this work. We also thank Aaron Johnson and Paul Lasky for their correspondences about the different memory waveform models. Furthermore, we thank Marc Favata for helpful comments on the manuscript. O. M. B. acknowledges funding from Vici research program "ARGO" with Project No. 639.043.815, financed by the Dutch Research Council (NWO). D. A. N. acknowledges the support of the Netherlands Organization for Scientific Research through the NWO VIDI Grant No. 639.042.612-Nissanke. P. S. acknowledges NWO Veni Grant No. 680-47-460. This paper has LIGO document number P2000013.

Note added.—Recently, a paper by Hübner *et al.* [33] appeared that estimated the number of BBH observations required to detect the nonlinear GW memory effect in BBH populations. There were several differences in methodology between this paper and [33]. First, [33] computed evidence ratios for signal hypotheses including and omitting the GW memory effect and the Bayes factor (BF) for the presence versus the absence of the memory effect in the population of BBHs (rather than computing the total SNR for the memory effect, as was done in this paper). Second, they used the higher-mode model rather than the quadrupole model as the fiducial waveform model for the GW

memory effect. Third, they use a different model for the population of BBHs: namely, model B of [32] for a specific set of parameters given in [33]. Fourth, they do not exclude events for which the sign of the GW memory effect is not well determined. With these differences in methodology, they find 1830^{+1730}_{-1100} detections (errors are 90% confidence intervals) are needed to reach a $\log \mathrm{BF} = 8$ for the GW memory effect.

A direct comparison of our results will require additional future work. As a rough comparison, we computed the number of detections needed to reach a total memory SNR $\langle \rho_{\rm tot} \rangle = 3$ for the same population as in [33] using their same waveform model for the GW memory effect. We find we need 1488^{+725}_{-879} (errors are 90% confidence intervals) to reach our SNR threshold. Thus, the results seem roughly consistent.

APPENDIX A: QUADRUPOLE KLUDGE MEMORY WAVEFORM MODEL

In this Appendix, we discuss one additional waveform model that was recently used in [24] to make estimates of the SNR for the GW memory effect in a wide range of GW detectors. We show that it produces a signal related to the GW memory effect that is roughly half the amplitude of the curves shown in Fig. 1, and which will also have some small oscillatory part that would typically not be expected in the corresponding spherical-harmonic modes for the memory.

The model of [24] begins with the procedure in [22], which proposed a method to simplify evaluating the angular integrals that appear in Eq. (2.6). The method is to compute the GW polarizations [similarly to what was done in Eq. (2.7)], but to work in coordinates adapted to the detector and the incoming radiation rather than the source. These coordinates are defined by choosing as the x direction any direction that is transverse to the vector pointing between the detector and the source. The GW polarizations are then computed with respect to the complex combination $e^{ij}_{+} + i e^{ij}_{\times}$ of polarization tensors, where $e^{ij}_{+} = (\hat{x}^i \hat{x}^j - \hat{y}^i \hat{y}^j)/2$ and $e^{ij}_{\times} = (\hat{x}^i \hat{y}^j + \hat{y}^i \hat{x}^j)/2$, and where $\hat{x}^i$ and $\hat{y}^i$ are unit vectors in the x and y directions, respectively, in the frame described in [22]. This simplifies the part of the integral proportional to $n'_j n'_k/(1 - \mathbf{n}' \cdot \mathbf{n})$ [although potentially at the expense of complicating the expansion of $dE/(d\Omega' du)$, which we had previously been computing in terms of multipole moments of the GW strain in coordinates in which the binary is in the x-y plane].

Johnson *et al.* [24] compute the GW polarizations following [22]. Rather than working out the detailed transformation of the multipole expansion of the luminosity per solid angle between the source coordinates and their coordinates for each line of sight from source to detector, they make the following approximate model that they describe as a "kludge": They take the angular dependence of the memory given in Eq. (2.11) [i.e., $\sin^2\iota(17 + \cos^2\iota)$], but instead of multiplying by the integral of $|\dot{h}_{22}|$ as in Eq. (2.11), they multiply by the integral of $\dot{h}^2_{+}$ evaluated at an inclination of $\iota = 0$ in the *source* coordinates, where h_{+} is the full plus polarization, including (in principle) all (ℓ, m) modes [as in Eq. (2.2)]. See [24] for the details about the rationale behind this prescription. This procedure leads to a real GW strain, which in the coordinates of [22] implies that the GW memory strain is plus polarized and is given by

$$h^{(\mathrm{K})}_{\mathrm{mem},+}(u) = \frac{r}{68\pi}\Phi(\iota)\int_{-\infty}^{u} \dot{h}^2_{+}|_{\iota=0} du'. \tag{A1}$$

We have defined $\Phi(\iota) = \sin^2(\iota)(17 + \cos^2\iota)$ for convenience.

For the inclination and phase ϕ_c that points to the line of sight to the detector, the polarizations e_{+} and $e_{\times}$ defined in the source coordinates in Eq. (2.8) are transverse (and traceless) tensors with respect to the direction of the line of sight. Thus, these polarizations in the source coordinates and those in the coordinates of [22] must be related by a rotation about the line of sight between the source and detector. In the quadrupole approximation in Sec. II D, the memory is plus polarized, but it is also plus polarized in Eq. (A1); thus, at this level of approximation for computing the GW polarizations associated with the GW memory effect, the rotation is trivial and the two sets of polarizations are equivalent.

Let us then write the integral in Eq. (A1) using the quadrupole approximation that only h_{22} contributes to $\dot{h}_{+}$ in the integral in Eq. (A1). We will denote this further approximation by $h^{(\mathrm{QK})}_{\mathrm{mem},+}(u)$. A straightforward calculation shows that the memory computed via the kludge method of [24] relates to the plus polarization of the GW memory effect in the quadrupole approximation in Eq. (2.11) as follows:

$$\begin{aligned} h^{(\mathrm{QK})}_{\mathrm{mem},+}(u) &= \frac{24}{17}|{}^{(-2)}Y_{22}(0,0)|^2 h^{\mathrm{mem}}_{+}(u) \\ &\quad + \frac{r}{136\pi}\Phi(\iota)\int_{-\infty}^{u} du' \mathrm{Re}\{[\dot{h}_{22}\,{}^{(-2)}Y_{22}(0,\phi_c)]^2\} \\ &\approx 0.56 h^{\mathrm{mem}}_{+}(u) \\ &\quad + \frac{r}{136\pi}\Phi(\iota)\int_{-\infty}^{u} du' \mathrm{Re}\{[\dot{h}_{22}\,{}^{(-2)}Y_{22}(0,\phi_c)]^2\}. \end{aligned} \tag{A2}$$

The second term involving the integral of the square of the real part of $\dot{h}_{22}$ will generally be small (see, e.g., [15]), and will oscillate at twice the frequency of the mode h_{22} (this is likely the origin of the oscillations in the memory waveform model in [24]). Thus, the quadrupole approximation to the procedure in [24] will typically produce a waveform that is roughly half the amplitude of the two models that use fewer approximations in Sec. II D, and it will contain an

additional unexpected oscillatory part. As a result, we do not include it in our comparison in Sec. II D.

APPENDIX B: ANALOGY BASED ON STACKING MEMORY SIGNALS

There is a simple analogy one can make to describe why it is important to know the sign of the GW memory effect to compute the total SNR in a population of BBHs. This is illustrated in Fig. 5 for four memory signals. It shows in the top panel that if the sign of the memory signals are known, then when N_e memory signals are added together the net signal will be roughly N_e times the individual signals, assuming the signals are on roughly the same size. The bottom panel shows that this does not occur when the GW memory waveforms are added with different signs. When N_e realizations of independent Gaussian noise are added together, the variance grows like N_e. Thus, the SNR grows like $\sqrt{(N_e)^2/N_e} = \sqrt{N_e}$ when the signals are added with the same sign, but it exhibits much slower (if any growth) with N_e if they are added with random signs.

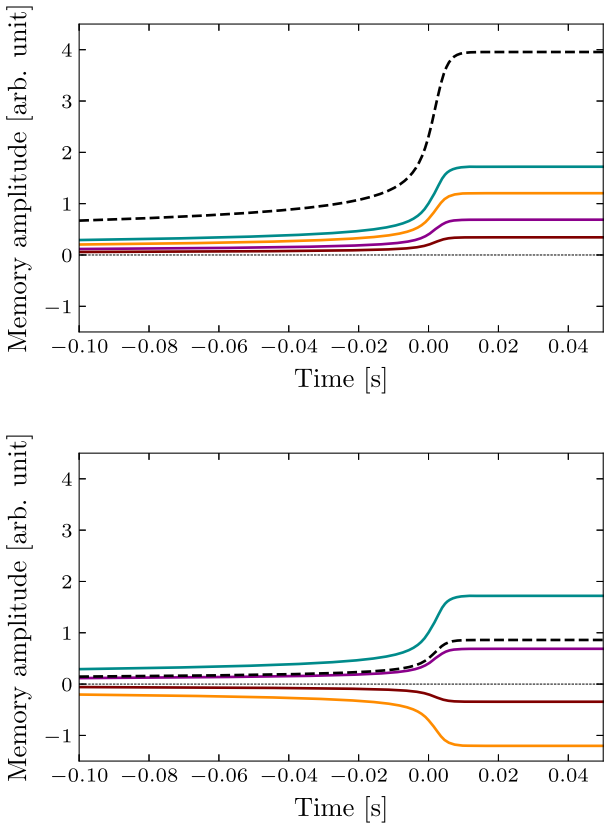

FIG. 5. Schematic illustration of why it is necessary to know the sign of the GW memory effect. The solid cyan, orange, purple, and brown curves are four GW memory waveforms. The dashed black curve is the sum of the waveforms. Top: We assume we know the sign of the GW memory for all events, so that when we add the individual events together, the combined signal is roughly 4 times larger than the average size of the individual signals. Bottom: We assume we do not know the sign of the GW memory, so that when we add the different waveforms, the ones with opposite sign cancel and the combined signal is on the same order as the individual waveforms.

APPENDIX C: A SECOND EXAMPLE OF DETERMINING THE SIGN OF THE MEMORY EFFECT

Here, we illustrate an example of a binary for which the sign of the GW memory effect is more challenging to measure than in the more typical example in Sec. IV A. We perform Bayesian inference as described in Sec. III C on a $m_1 = 30M_\odot$, $m_2 = 20M_\odot$ binary at a fixed luminosity distance $d_L = 500$ Mpc. Here, we now vary $\rho_N^{\rm hom}$ by changing the inclination ι rather than the luminosity distance d_L. In Fig. 6 (going clockwise from the top left) are the distributions of the inner product $\langle h_{\rm mem}(\vec{\theta}_{\rm true})|h_{\rm mem}(\vec{\theta}_s)\rangle$ for $\iota = 3.0$, 0.3, 0.48, and 2.4 (where the SNRs $\rho_N^{\rm hom}$ are given by 1, 2, 3, and 4). The oscillatory SNR for the three detector network is above the threshold for detection for all four inclination angles. The histograms for Advanced Virgo, LIGO Hanford, and LIGO Livingston are shown in orange, green, and blue, respectively.

When there is an SNR of 2 in the higher-order modes, there is more support for the true sign of the memory effect in the Virgo detector than in the two LIGO detectors. This occurs for the following reasons: First, the LIGO antenna patterns are not very sensitive to the plus polarization for the sky location and polarization of the binary. Furthermore, the source is located almost directly above the plane formed by the three detectors, and there is an approximate degeneracy between the true location of the source and the source on the opposite side of the sky. Thus, there is an additional degeneracy between the sky location and polarization in addition to the degeneracy between the polarization and phase ϕ_c. These facts combine to require a slightly higher SNR of closer to 3 in the higher-order modes before the sign of the memory is more confidently measured by Virgo and LIGO Livingston (LIGO Hanford is not sensitive to the plus polarization of the binary). This case is somewhat unusual, because of the very specific sky location and polarization leading to a poor sensitivity to the GW memory in the LIGO detectors; the results in Fig. 2 are more representative of most binaries that we simulated.

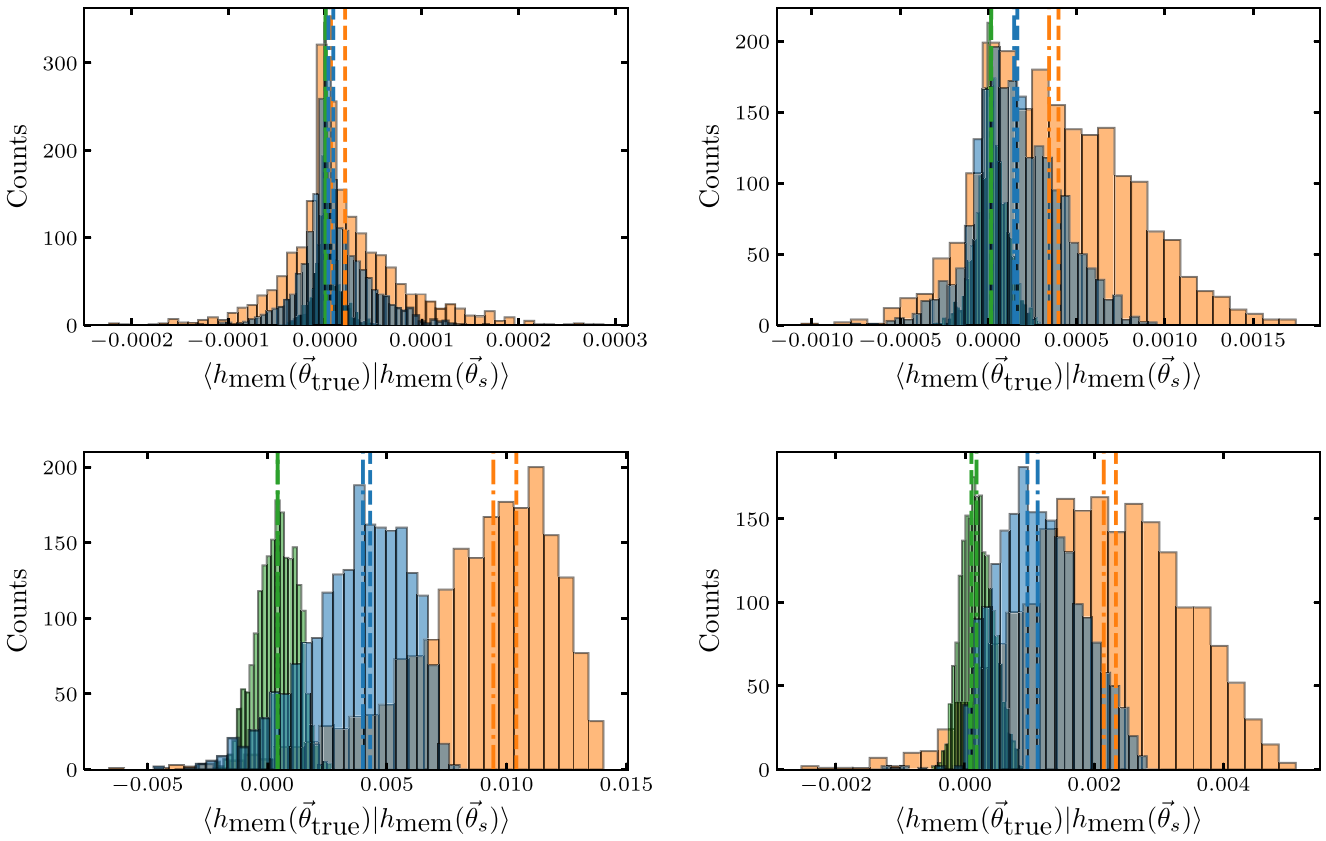

FIG. 6. Distribution of noise-weighted inner products for the memory effect for a nonspinning binary with $m_1 = 30M_\odot$, $m_2 = 20M_\odot$ at a fixed luminosity distance $d_L = 500$ Mpc with sky location and polarization given by $\alpha = 2.3$ rad, $\delta = 1.0$ rad and $\psi = 0.3$ rad. As in Fig. 2, this figure shows the inner product of the true signal with template waveforms that are consistent with the posterior PDFs: $\langle h_{\rm mem}(\vec{\theta}_{\rm true})|h_{\rm mem}(\vec{\theta}_s)\rangle$. Advanced LIGO Hanford, LIGO Livingston and Virgo are shown in green, blue and orange, respectively. The vertical dashed lines represent the injected values of the optimal SNR squared, and the vertical dot-dashed lines represent the median values of the distributions. Here the SNR in the higher-order modes $\rho_N^{\rm hom}$ is approximately 1, 2, 3, and 4 going clockwise from the top left. These different SNRs were achieved just by varying the inclination angle of the source (the specific values are given in the text).

[1] B. P. Abbott *et al.* (LIGO Scientific and Virgo Collaborations), Observation of Gravitational Waves from a Binary Black Hole Merger, Phys. Rev. Lett. **116**, 061102 (2016).

[2] B. P. Abbott *et al.* (LIGO Scientific and Virgo Collaborations), Tests of General Relativity with GW150914, Phys. Rev. Lett. **116**, 221101 (2016); Erratum, Phys. Rev. Lett. **121**, 129902 (2018).

[3] B. P. Abbott *et al.* (LIGO Scientific and Virgo Collaborations), GWTC-1: A Gravitational-Wave Transient Catalog of Compact Binary Mergers Observed by LIGO and Virgo during the First and Second Observing Runs, Phys. Rev. X **9**, 031040 (2019).

[4] B. P. Abbott *et al.* (LIGO Scientific and Virgo Collaborations), Tests of general relativity with the binary black hole signals from the LIGO-Virgo catalog GWTC-1, Phys. Rev. D **100**, 104036 (2019).

[5] GraceDB: Gravitational-wave candidate event database, https://gracedb.ligo.org/latest/.

[6] D. Shoemaker (LIGO Scientific Collaboration), Gravitational wave astronomy with LIGO and similar detectors in the next decade, arXiv:1904.03187.

[7] C. M. Will, The confrontation between general relativity and experiment, Living Rev. Relativity **17**, 4 (2014).

[8] D. Christodoulou, Nonlinear Nature of Gravitation and Gravitational Wave Experiments, Phys. Rev. Lett. **67**, 1486 (1991).

[9] L. Blanchet and T. Damour, Hereditary effects in gravitational radiation, Phys. Rev. D **46**, 4304 (1992).

[10] Y. B. Zel'dovich and A. G. Polnarev, Astron. Zh. **51**, 30 (1974) [Radiation of gravitational waves by a cluster of superdense stars, Sov. Astron. **18**, 17 (1974)].
[11] E. T. Newman and R. Penrose, Note on the Bondi-Metzner-Sachs group, J. Math. Phys. (N.Y.) **7**, 863 (1966).
[12] R. Epstein, The generation of gravitational radiation by escaping supernova neutrinos, Astrophys. J. **223**, 1037 (1978).
[13] M. S. Turner, Gravitational radiation from supernova neutrino bursts, Nature (London) **274**, 565 (1978).
[14] A. G. Wiseman and C. M. Will, Christodoulou's nonlinear gravitational wave memory: Evaluation in the quadrupole approximation, Phys. Rev. D **44**, R2945 (1991).
[15] M. Favata, Post-Newtonian corrections to the gravitational-wave memory for quasicircular, inspiralling compact binaries, Phys. Rev. D **80**, 024002 (2009).
[16] D. Pollney and C. Reisswig, Gravitational memory in binary black hole mergers, Astrophys. J. **732**, L13 (2011).
[17] H. Bondi, M. G. J. van der Burg, and A. W. K. Metzner, Gravitational waves in general relativity. VII. Waves from axi-symmetric isolated systems, Proc. R. Soc. A **269**, 21 (1962).
[18] R. K. Sachs, Gravitational waves in general relativity. VIII. Waves in asymptotically flat space-time, Proc. R. Soc. A **270**, 103 (1962).
[19] R. Sachs, Asymptotic symmetries in gravitational theory, Phys. Rev. **128**, 2851 (1962).
[20] A. Strominger, Lectures on the infrared structure of gravity and gauge theory, arXiv:1703.05448.
[21] M. Favata, Nonlinear gravitational-wave memory from binary black hole mergers, Astrophys. J. **696**, L159 (2009).
[22] K. S. Thorne, Gravitational-wave bursts with memory: The Christodoulou effect, Phys. Rev. D **45**, 520 (1992).
[23] D. Kennefick, Prospects for detecting the Christodoulou memory of gravitational waves from a coalescing compact binary and using it to measure neutron star radii, Phys. Rev. D **50**, 3587 (1994).
[24] A. D. Johnson, S. J. Kapadia, A. Osborne, A. Hixon, and D. Kennefick, Prospects of detecting the nonlinear gravitational wave memory, Phys. Rev. D **99**, 044045 (2019).
[25] M. Punturo *et al.*, The Einstein Telescope: A third-generation gravitational wave observatory, Classical Quantum Gravity **27**, 194002 (2010).
[26] D. Reitze *et al.*, Cosmic explorer: The U.S. contribution to gravitational-wave astronomy beyond LIGO, Bull. Am. Astron. Soc. **51**, 035 (2019).
[27] P. Amaro-Seoane *et al.* (LISA Collaboration), Laser interferometer space antenna, arXiv:1702.00786.
[28] G. Hobbs and S. Dai, Gravitational wave research using pulsar timing arrays, Natl. Sci. Rev. **4**, 707 (2017).
[29] K. Aggarwal *et al.* (NANOGrav Collaboration), The NANOGrav 11-Year data set: Limits on gravitational wave memory, Astrophys. J. **889**, 38 (2019).
[30] K. Islo, J. Simon, S. Burke-Spolaor, and X. Siemens, Prospects for memory detection with low-frequency gravitational wave detectors, arXiv:1906.11936.
[31] P. D. Lasky, E. Thrane, Y. Levin, J. Blackman, and Y. Chen, Detecting Gravitational-Wave Memory with LIGO: Implications of GW150914, Phys. Rev. Lett. **117**, 061102 (2016).
[32] B. P. Abbott *et al.* (LIGO Scientific and Virgo Collaborations), Binary black hole population properties inferred from the first and second observing runs of Advanced LIGO and Advanced Virgo, Astrophys. J. **882**, L24 (2019).
[33] M. Hübner, C. Talbot, P. D. Lasky, and E. Thrane, Thanks for the memory: Measuring gravitational-wave memory in the first LIGO/Virgo gravitational-wave transient catalog, Phys. Rev. D **101**, 023011 (2020).
[34] M. Favata, The gravitational-wave memory effect, Classical Quantum Gravity **27**, 084036 (2010).
[35] C. Talbot, E. Thrane, P. D. Lasky, and F. Lin, Gravitational-wave memory: Waveforms and phenomenology, Phys. Rev. D **98**, 064031 (2018).
[36] P. A. R. Ade *et al.* (Planck Collaboration), Planck 2015 results. XIII. Cosmological parameters, Astron. Astrophys. **594**, A13 (2016).
[37] W. G. Anderson, P. R. Brady, J. D. E. Creighton, and E. E. Flanagan, An excess power statistic for detection of burst sources of gravitational radiation, Phys. Rev. D **63**, 042003 (2001).
[38] LIGO Scientific Collaboration, LIGO Algorithm Library—LALSuite, free software (GPL) (2019).
[39] S. Field, C. Galley, and J. Blackman, gwsurrogate python package, https://pypi.org/project/gwsurrogate/.
[40] A. Lewis, A. Challinor, and N. Turok, Analysis of CMB polarization on an incomplete sky, Phys. Rev. D **65**, 023505 (2001).
[41] E. Berti, V. Cardoso, J. A. Gonzalez, U. Sperhake, M. Hannam, S. Husa, and B. Bruegmann, Inspiral, merger, and ringdown of unequal mass black hole binaries: A multipolar analysis, Phys. Rev. D **76**, 064034 (2007).
[42] V. Varma, S. E. Field, M. A. Scheel, J. Blackman, L. E. Kidder, and H. P. Pfeiffer, Surrogate model of hybridized numerical relativity binary black hole waveforms, Phys. Rev. D **99**, 064045 (2019).
[43] M. Boyle *et al.*, The SXS collaboration catalog of binary black hole simulations, Classical Quantum Gravity **36**, 195006 (2019).
[44] P. Ajith *et al.*, Phenomenological template family for black-hole coalescence waveforms, Classical Quantum Gravity **24**, S689 (2007).
[45] L. Blanchet, Gravitational radiation from post-Newtonian sources and inspiralling compact binaries, Living Rev. Relativity **17**, 2 (2014).
[46] A. Buonanno and T. Damour, Effective one-body approach to general relativistic two-body dynamics, Phys. Rev. D **59**, 084006 (1999).
[47] A. Bohé *et al.*, Improved effective-one-body model of spinning, nonprecessing binary black holes for the era of gravitational-wave astrophysics with advanced detectors, Phys. Rev. D **95**, 044028 (2017).
[48] S. E. Field, C. R. Galley, J. S. Hesthaven, J. Kaye, and M. Tiglio, Fast Prediction and Evaluation of Gravitational Waveforms using Surrogate Models, Phys. Rev. X **4**, 031006 (2014).
[49] K. Cannon, J. D. Emberson, C. Hanna, D. Keppel, and H. Pfeiffer, Interpolation in waveform space: Enhancing the accuracy of gravitational waveform families using numerical relativity, Phys. Rev. D **87**, 044008 (2013).

[50] M. Pürrer, Frequency domain reduced order models for gravitational waves from aligned-spin compact binaries, Classical Quantum Gravity **31**, 195010 (2014).
[51] J. Blackman, S. E. Field, C. R. Galley, B. Szilágyi, M. A. Scheel, M. Tiglio, and D. A. Hemberger, Fast and Accurate Prediction of Numerical Relativity Waveforms from Binary Black Hole Coalescences Using Surrogate Models, Phys. Rev. Lett. **115**, 121102 (2015).
[52] J. Blackman, S. E. Field, M. A. Scheel, C. R. Galley, D. A. Hemberger, P. Schmidt, and R. Smith, A surrogate model of gravitational waveforms from numerical relativity simulations of precessing binary black hole mergers, Phys. Rev. D **95**, 104023 (2017).
[53] N. T. Bishop, R. Gomez, L. Lehner, and J. Winicour, Cauchy-characteristic extraction in numerical relativity, Phys. Rev. D **54**, 6153 (1996).
[54] D. A. Nichols, Spin memory effect for compact binaries in the post-Newtonian approximation, Phys. Rev. D **95**, 084048 (2017).
[55] A. Ashtekar, T. De Lorenzo, and N. Khera, Compact binary coalescences: Constraints on waveforms, arXiv:1906.00913.
[56] G. Compère, R. Oliveri, and A. Seraj, The Poincaré and BMS flux-balance laws with application to binary systems, arXiv:1912.03164.
[57] G. Faye, L. Blanchet, and B. R. Iyer, Non-linear multipole interactions and gravitational-wave octupole modes for inspiralling compact binaries to third-and-a-half post-Newtonian order, Classical Quantum Gravity **32**, 045016 (2015).
[58] T. Damour, A. Nagar, M. Hannam, S. Husa, and B. Bruegmann, Accurate effective-one-body waveforms of inspiralling and coalescing black-hole binaries, Phys. Rev. D **78**, 044039 (2008).
[59] H. Yang and D. Martynov, Testing Gravitational Memory Generation with Compact Binary Mergers, Phys. Rev. Lett. **121**, 071102 (2018).
[60] C. Talbot, gwmemory python package, https://github.com/ColmTalbot/gwmemory.
[61] D. J. A. McKechan, C. Robinson, and B. S. Sathyaprakash, A tapering window for time-domain templates and simulated signals in the detection of gravitational waves from coalescing compact binaries, Classical Quantum Gravity **27**, 084020 (2010).
[62] J. W. Cooley and J. W. Tukey, An algorithm for the machine calculation of complex Fourier series, Math. Comput. **19**, 297 (1965).
[63] T. E. Oliphant, *Guide to NumPy: 2nd Edition* (Continuum Press, Austin, 2015).
[64] S. van der Walt, S. C. Colbert, and G. Varoquaux, The numpy array: A structure for efficient numerical computation, Comput. Sci. Eng. **13**, 22 (2011).
[65] C. Cutler and E. E. Flanagan, Gravitational waves from merging compact binaries: How accurately can one extract the binary's parameters from the inspiral wave form? Phys. Rev. D **49**, 2658 (1994).
[66] P. B. Graff, A. Buonanno, and B. S. Sathyaprakash, Missing link: Bayesian detection and measurement of intermediate-mass black-hole binaries, Phys. Rev. D **92**, 022002 (2015).
[67] E. Payne, C. Talbot, and E. Thrane, Higher order gravitational-wave modes with likelihood reweighting, Phys. Rev. D **100**, 123017 (2019).
[68] L. London, S. Khan, E. Fauchon-Jones, C. García, M. Hannam, S. Husa, X. Jiménez-Forteza, C. Kalaghatgi, F. Ohme, and F. Pannarale, First Higher-Multipole Model of Gravitational Waves from Spinning and Coalescing Black-Hole Binaries, Phys. Rev. Lett. **120**, 161102 (2018).
[69] P. Kumar, J. Blackman, S. E. Field, M. Scheel, C. R. Galley, M. Boyle, L. E. Kidder, H. P. Pfeiffer, B. Szilagyi, and S. A. Teukolsky, Constraining the parameters of GW150914 and GW170104 with numerical relativity surrogates, Phys. Rev. D **99**, 124005 (2019).
[70] K. Chatziioannou *et al.*, On the properties of the massive binary black hole merger GW170729, Phys. Rev. D **100**, 104015 (2019).
[71] L. S. Finn, Detection, measurement and gravitational radiation, Phys. Rev. D **46**, 5236 (1992).
[72] J. Aasi *et al.* (LIGO Scientific Collaboration), Advanced LIGO, Classical Quantum Gravity **32**, 074001 (2015).
[73] F. Acernese *et al.* (Virgo collaboration), Advanced Virgo: A second-generation interferometric gravitational wave detector, Classical Quantum Gravity **32**, 024001 (2015).
[74] B. P. Abbott *et al.* (LIGO Scientific and Virgo Collaborations), Properties of the Binary Black Hole Merger GW150914, Phys. Rev. Lett. **116**, 241102 (2016).
[75] T. Bayes, An essay toward solving a problem in the doctrine of chances, Phil. Trans. R. Soc. London **53**, 370 (1764).
[76] E. T. Jaynes, *Probability Theory: The Logic of Science*, edited by G. L. Bretthorst (Cambridge University Press, Cambridge, England, 2003).
[77] J. Veitch *et al.*, Parameter estimation for compact binaries with ground-based gravitational-wave observations using the LALInference Software library, Phys. Rev. D **91**, 042003 (2015).
[78] B. Farr and W. M. Farr, kombine: A kernel-density-based, embarrassingly parallel ensemble sampler, https://github.com/bfarr/kombine (to be published).
[79] GW Observatory Status, https://www.gw-openscience.org/detector_status/.
[80] https://doi.org/10.5281/zenodo.3724442.